國立臺灣大學工學院材料科學與工程學研究所

碩士論文

Department of Materials Science and Engineering

College of Engineering

National Taiwan University

Master Thesis

Al 的添加與氮化作用對於 NbTiVZr 高熵合金薄膜之顯微結構差異與機械性質探討

Effects of Al Addition and Nitridation on Microstructures and Mechanical Properties of NbTiVZr High entropy alloy Films

張洛齊

Lo Chi Chang

指導教授：薛承輝 博士

Advisor: Chun Hway Hsueh, Ph.D.

中華民國 112 年 3 月

March, 2023

doi:10.6342/NTU202300667

誌謝

碩士班兩年的時間過得好快，還依稀記得兩年前的四月中剛到實驗室，每天找學長姐學習儀器的時光，轉眼間，就已經到了在自己在準備碩班口試與寫論文的日子，這兩年中受到很多人的幫助，在此我想一一道謝。首先，我想謝謝我的指導教授薛承輝老師願意給我這個機會加入 MMLAB 這個大家庭，老師提供給我們實驗室非常自由的研究環境，老師曾說過，他當初在當研究生的時候不喜歡被限制研究內容與走向，因此他也不希望太過限制我們研究生的研究方向。在這兩年的時間，我的研究過程並非順遂，嘗試了幾種不同題目，常常花了許多心力在某個實驗上卻沒什麼進展，但老師都會鼓勵我並且支持我想做的研究。不僅如此，當老師聽到我之後想要出國當交換生時，也是很鼓勵我出國多看看，我很感激當初有加入老師的實驗室，也受惠無窮。非常感謝楊哲人教授與郭俞麟教授在百忙之中還願意撥空前來擔任我的口試委員，並且願意給我許多研究上的建議，使我的論文能夠更完整。

謝謝 MMLAB 裡的研究夥伴，謝謝黎佳霖學長能在我研究上提供大大小小的幫助，並在我在研究上的給一些提點，希望學長之後找教職順利。謝謝盈州學長幫我拍 TEM，學長拍 TEM 的技術真的是無話可說，而且學長人超 nice，又愛喝可不可跟吃樂澄小舖牛肉麵。謝謝實驗室的品潔、宜亭、舒霓、馨薇學姊在我碩一那年，耐心教會我各種實驗，特別是鍍膜機與 NOVA，也希望學姊們能在之後的工作上都能順利。謝謝同屆的三位好夥伴瑋哲、逸翔與亮言兩年的陪伴，共同分擔實驗室大大小小的事務，一起修碩士班繁雜的課，一起做研究。謝謝實驗室學弟妹慧文、梁容、振德、宛儀、亦羚為實驗室注入滿滿的活力，也一起分擔許多實驗室內各種的事物，祝你們在未來研究上能夠順利畢業。特別感謝振德在我的研究上幫忙很多，包含 XPS 與 Nano-scratch 的實驗，這段期間收穫非常多，也非常感激，祝你跟韓國女友能夠順利。謝謝踵智學長負責實驗室的衛生，會主動清冰箱跟掃地，又很會健身，祝學長順利畢業。謝謝其他實驗室的好夥伴映竹、懿霆一起陪我度過兩年碩班時光，常常會一起吃飯聊天打壁球跟籃球，聊了許多生活上不如意的事!

doi:10.6342/NTU202300667

最後，我要特別感謝我的家人，謝謝我的父母，對我從小到大的栽培，並且提供給我完善的學習環境，在我碩班研究的這段時間，能夠專心在研究上，不用為了生活而煩惱。謝謝我的姊姊，能夠在我失落不如意的時候，提供給我一個避風港，並且支持我的決定。對於我未提及但過去曾經幫助過我的人，我也在此奉上我最大的感謝，謝謝你們。

張洛齊 謹誌

於國立台灣大學材料科學與工程學系研究所

2022 年 7 月 14 日

doi:10.6342/NTU202300667

中文摘要

本實驗透過磁控濺鍍系統，製備一系列$(NbTiVZr)_{100-x}Al_x$ (x=0, 3.5, 7.3, 12.4, 12.9)高熵合金薄膜與$(NbTiVZrN)_{100-x}Al_x$ (x=0, 0.7, 2.3, 3.6, 4.0)高熵合金氮化薄膜，並且以雙靶材共鍍的方式，鍍在單晶矽(100)上，透過調控施加在鋁靶材上不同的功率，並且固定其他參數，去探討 Al 的添加量對 NbTiVZr 高熵合金薄膜與氮化薄膜之微結構差異與機械性質的探討。在高熵合金薄膜結果方面，從 X 光繞射儀與穿透式電子顯微鏡的結果中可看出，所有薄膜皆為非晶結構，從選區繞射圖型可以看到明顯的非晶環，在掃描式電子顯微鏡下則可以發現所有試片皆為葉脈狀結構，而這結構也是在非晶相中最常出現的結構之一。

高熵合金氮化薄膜的討論中，在 X 光繞射儀與穿透式電子顯微鏡的結果中發現在未添加鋁的薄膜中，主要是由氮化鈦 (TiN) 主導，並且在電子顯微鏡的橫截面圖形出現雙層結構，上層為柱狀晶結構而下層則是非晶的結構，而非晶結構也在後續高解析電子顯微鏡被驗證為奈米晶散落在非晶母相中。隨著鋁的添加後，由於鋁與鈦的混和焓 (mixing enthalpy) 很負因而形成三鈦化鋁 (Ti_3Al)，導致氮轉而與鈮與鋯結合，分別形成氮化鈮 (NbN) 與氮化鋯 (ZrN)，這兩種氮化物主導了添加鋁氮化薄膜的結構與其優異的機械性質。這也在後續的X射線光電子能譜儀 (XPS) 結果中被驗證。機械性質方面，本實驗量測硬度、破裂韌性與摩擦係數。結果顯示，隨著鋁含量添加至 x=3.6 時，硬度與破裂韌性分別達到最大值，其原因可歸因於固溶強化與主導之氮化物的轉變。在奈米刮痕方面，隨著鋁的添加，所得摩擦係數從 0.082 降到 0.065，因此可知鋁的添加強化高熵合金氮化薄膜的磨耗性質。

關鍵字: 高熵合金薄膜、氮化膜、磁控濺鍍、機械性質、鋁添加

doi:10.6342/NTU202300667

ABSTRACT

In this study, the effects of Al addition on the phase evolution, morphology and mechanical properties of $(NbTiVZr)_{100-x}Al_x$ (x = 0, 3.5, 7.3, 12.4, 12.9) high entropy alloy films (HEAFs) and $(NbTiVZrN)_{100-x}Al_x$ (x=0, 0.7, 2.3, 3.6, 4.0) high entropy alloy nitride films (HEANFs) were systematically investigated. For the $(NbTiVZr)_{100-x}Al_x$ HEAFs, all the films exhibited amorphous structure and the hardness increased slightly. For the nitride films, the XRD patterns revealed FCC structure and the preferred orientation transferred from TiN(200) to (Nb, Zr)N(111) as the Al content increased. The results of the corresponding selected-area electron diffraction patterns of TEM images agreed well with the XRD results. Cross-sectional SEM and TEM observations exhibited ultra-fine columnar structure with a few inclusions and voids. XPS was conducted in order to further investigate the bonding between the constituent elements, and the replacement of the dominant compounds was confirmed. The nanoindentation test were performed to acquire the mechanical properties of the films. The hardness, reduced modulus and fracture toughness of nitride film increased with the increasing Al concentration and reached the maximum values of 28.1 GPa, 253 GPa and 2.08 MPa×$m^{0.5}$, respectively, for x = 3.6. The significant improvement could be ascribed to solid solution strengthening, inverse Hall-Petch effect and the replacement of dominant nitride compounds. As the Al content increased to x = 4.0, the coefficient of friction decreased from 0.082 to 0.065. The relationship between the microstructure and mechanical properties was studied for the $(NbTiVZrN)_{100-x}Al_x$ HEANFs in this work.

Keywords: high entropy alloy films; Al addition; nitride films; microstructure; mechanical properties

doi:10.6342/NTU202300667

CONTENTS

doi:10.6342/NTU202300667

doi:10.6342/NTU202300667

LIST OF FIGURES

doi:10.6342/NTU202300667

doi:10.6342/NTU202300667

doi:10.6342/NTU202300667

LIST OF TABLES

doi:10.6342/NTU202300667

Chapter 1 Introduction

High-entropy alloys (HEAs), first reported by Yeh et al. in 2004 [1], differ from conventional alloys by containing five or more principal elements with each concentration between 5 and 35 at.%. Due to the four core effects, namely high mixing entropy, sluggish diffusion, severe lattice distortion and cocktail effect, HEAs are generally favorable to form simple BCC, FCC solid solutions or amorphous phase [2, 3]. Much attention has been attracted to the investigation of bulk HEAs prepared by arc melting and casting; however, high entropy alloy films (HEAFs) have also attracted broad interest over the last decade due to their excellent mechanical properties. Compared to bulk HEA materials fabricated by casting, HEAFs fabricated by magnetron sputtering [4-8] are subjected to the much faster cooling rate that would limit the diffusion of elements and inhibit the grain growth to obtain the much smaller grain sizes. It is also more likely to form the amorphous phase or the metastable solid solution without the presence of any precipitates for HEAFs [9-12].

Since the 2010s, high-entropy alloy nitride films (HEANFs) have received much attention due to their attractive mechanical properties, such as high hardness [13, 14], excellent electrical properties [15], corrosion resistances [16] and creep behaviors [17]. Those superior mechanical properties are attributed to the formation of mixed ion-metal-covalent bonds. Cui et al. [18] prepared the (AlCrTiZrHf)N films using radio frequency

doi:10.6342/NTU202300667

(RF) magnetron sputtering. As the nitrogen content increased from 0 to ~50 at.%, the hardness was improved from 17.9 to 33.1 GPa. Chen et al. [19] reported that the AlCrMoTaTi HEANFs exhibited the maximum hardness of 34.0 GPa. In Chang et al.'s works [20], (CrTaTiVZr)N films deposited by magnetron sputtering possessed superior hardness of 36.6 GPa. Moreover, nitrides could serve as the heterogeneous nucleation sites for crystallization and thus the structure of HEANFs presented in existing works mostly exhibited highly crystallized grains [21, 22]. Liang et al. [23] and Chang et al. [24] fabricated the (TiVCrZrHf)N and TiVCrAlZr HEANFs, respectively, by reactive magnetron sputtering and the FCC structure was revealed in both researches. The structure of (CrAlTiNbV)N films reported by Lu et al. [25] also exhibited FCC phase as well.

Recently, more and more research efforts have been devoted to doping one or two elements in the HEAs with different concentrations in order to improve the mechanical performances [26-30]. In this study, four refractory metal elements Nb, Ti, V, Zr are selected based on the facts that these elements have the similar atomic size, electronegativity and sputter yield. In addition, the as-cast NbTiVZr HEA possess a high yield strength of 1320 MPa but poor compressive ductility of 4.2% [31]. Stepanov et al. [32] and Xu et al. [31] introduced aluminum to the NbTiVZr alloy system because Al has a negative mixing enthalpy with the constituent elements in NbTiVZr alloy (the mixing

doi:10.6342/NTU202300667

enthalpies of Al with Nb, Ti, V and Zr atomic pairs are –18, –30, –16, and –44 kJ/mol, respectively) [33]. The incorporation of Al in the NbTiVZr alloy successfully helped the $Al_{0.3}$NbTiVZr alloy to possess a higher yield strength of 1367 MPa and superior compressive ductility of 10.14%. Hsu et al. [34] studied the effects of Al doping on the microstructure and mechanical properties of Al_xCoCrFeMnNi HEAFs and found that the hardness of Al-doped HEAFs increased significantly from 5.71 to 8.74 GPa. Feng et al. [35] fabricated the Al_xCoCrFeNi HEAFs and found that with the Al addition, the structure changed from FCC to BCC and the hardness increased from 3.8 to 4.3 GPa.

The aim of the present study was to optimize the mechanical properties of the $(NbTiVZr)_{100-x}Al_x$ (x = 0, 3.5, 7.3, 12.4, 12.9) HEAFs and $(NbTiVZrN)_{100-x}Al_x$ (x=0, 0.7, 2.3, 3.6, 4.0) HEANFs and to observe the difference in microstructures with various Al concentrations. In this work, a series of $(NbTiVZr)_{100-x}Al_x$ HEAFs and $(NbTiVZrN)_{100-x}Al_x$ HEANFs was deposited by RF magnetron sputtering. The chemical compositions, crystalline structures, chemical bonding of the constituent elements and mechanical properties of the films were analyzed, and the correlation between the microstructures and mechanical properties was systematically investigated.

Chapter 2 Literature Review

2.1 High entropy alloys

Unlike most conventional alloy design strategy based on one or two principal

doi:10.6342/NTU202300667

metallic elements, high entropy alloys (HEAs), first introduced independently by Yeh et al. [1] and Cantor et al. [36] in 2004, has attracted lots of attention over the past decade. Due to the large mixing entropies among each element, HEAs are favorable to form solid solution, FCC, BCC structure or amorphous phase rather than intermetallic compounds [2, 3, 37]. Furthermore, the manufacturing process of HEAs doesn't require special techniques or equipment, which indicates that the fabrication of HEAs can be easily completed with existing equipment and technologies. With the four core effects, namely high mixing entropy, sluggish diffusion, severe lattice distortion and cocktail effect, HEAs possess a remarkable potential in hardness and strength [38-41], wear resistance [42-44], fracture toughness [45], corrosion resistance [46-48] and high temperature resistance [49-51], which shed light on the design of potential materials. As a result, HEAs have captured extensive attention and efforts of growing numbers in the materials science community in the past decade.

2.1.1 Definitions

According to the earlier researches published by Prof. Yeh et al. [1, 3], HEAs are defined as multicomponent alloys which composed of five or more principal elements in equimolar ratios. In order to expand the scope of alloy design, HEAs were defined as principal elements with the concentration of each element being between 5 to 35 at.%. The revised definition of HEAs doesn't need to be equimolar, which increases the

doi:10.6342/NTU202300667

possibility of HEAs design significantly [37]. The widely accepted definition of HEAs is based on two factors: chemical compositions and mixing entropies.

The configurational entropy of a system is calculated with the Boltzmann's equation [52] as follow:

$$\Delta S_{conf} = k_B \ln w \quad (1)$$

where k_B is Boltzmann's constant and w is the number distinguishable micro-states in the system. Following the Boltzmann's formula, when the solid solution is composed of n-element equimolar alloy, the molar mixing configurational entropy can be calculated with a simple approach [3]:

$$\Delta S_{conf} = R \ln n \quad (2)$$

where R = 8.314 J K^{-1} mol^{-1} and n is the number of the elements of the alloy and has to be larger than 5, resulting in the value of ΔS_{conf} must be larger than 13.37 J K^{-1} mol^{-1}. However, when the concentration of each element is not equimolar, the configurational entropy can also be acquired as [53, 54]:

$$\Delta S_{conf} = -R \sum_{i=1}^{n} X_i \ln X_i \quad (3)$$

where X_i is the atomic percentage for the ith element. Based on the equations above, the alloys were roughly grouped into three categories according to their mixing entropy in the random solution state shown in Fig. 2-1, namely

(i) Low-entropy alloys: $\Delta S_{conf} \leq 0.69R$, containing 1 or 2 as major elements;

doi:10.6342/NTU202300667

(ii) Medium-entropy alloys; $0.69R \leq \Delta S_{conf} \leq 1.61R$, containing 2–4 main elements;

(iii) High-entropy alloys: $\Delta S_{conf} \geq 1.61R$, containing at least 5 elements.

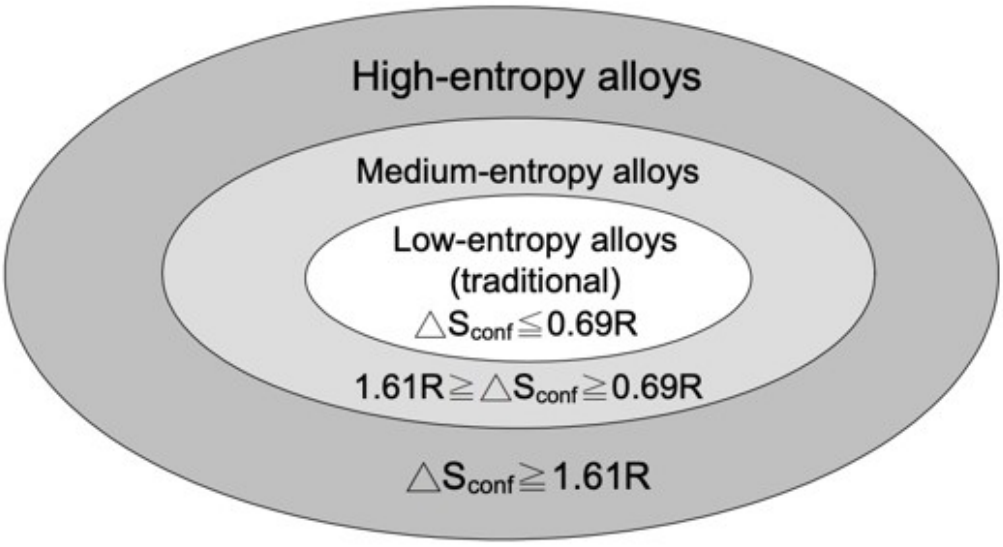

Fig. 2-1 The definition of high entropy alloys, medium entropy alloys and low entropy alloys [3].

2.1.2 Four Core Effects

Four core effects are often referred to describe HEAs, there are the high mixing entropy effect, sluggish diffusion effect, severe lattice distortion effect and cocktail effect [3]. Those hypotheses were first proposed based on information available in the earlier publications. The four core effects will be briefly introduced and evaluated in this section below.

High Entropy Effect

The high entropy effect is the representative concept of HEAs, proposing that the increased configurational entropy may favor the formation of the solid solution phase

doi:10.6342/NTU202300667

(FCC, BCC, HCP, amorphous etc.) over intermetallic compounds. For HEAs, the difference in entropy among constituent elements is particularly large owing to the multiprincipal-element design. The high entropy effect indicates that the higher mixing entropy in HEAs lowers the Gibbs free energy of solid solution phases and stabilizes the formation of solid solution, particularly at high temperatures. According to the following equation, the Gibb's free energy of mixing (ΔG_{mix}) of a solid solution is commonly used to predict the phase formation [54-56].

$$\Delta G_{mix} = \Delta H_{mix} - T\Delta S_{mix} \quad (4)$$

where ΔH_{mix} is the enthalpy of mixing, T is the temperature of the system and ΔS_{mix} is the entropy of mixing. Hence, the formation of solid solution phase depends on whether the value of $-T\Delta S_{mix}$ is smaller than ΔH_{mix}. While vibrational, electronic and magnetic terms are acknowledged, the configurational term is still considered to be dominant [37]. Despite the fact that the mixing enthalpy in solid solutions is relatively low compared to intermetallic compounds, the mixing entropy increases with the number of the elements which overcomes the loss of mixing enthalpy and therefore tend to the form the solid solution phases.

Severe Lattice Distortion Effect

Severe lattice distortion is attributed to the size difference of atoms that lead to the displacement of lattice sites [37, 57]. Larger atoms push away their neighbors and small

doi:10.6342/NTU202300667

ones have extra space around. With the sufficiently large atomic size differences, the distorted lattice may collapse into an amorphous structure since the lattice distortion energy would be too high to retain crystalline configuration. The distortion in either crystalline or amorphous structures influence the microstructure, properties, thermodynamics and kinetics of materials. Moreover, the difference of bonding energies and crystal structure tendencies results in higher lattice distortion due to the nonsymmetrical neighboring atoms.

Sluggish Diffusion Effect

It was proposed that the effective diffusion rate and phase transformation kinetics in HEAs are slower than those in pure metals and conventional alloys counterparts. The severe lattice distortion which hinders atomic movement will limit the effective diffusion rate and impede the transformation in HEAs [58, 59]. As a result, the slow-moving elements inhibited the phase separation and resulted in the solid solution phase rather than intermetallic phase.

Cocktail Effect

Cocktail effect is an evocative phrase first introduced by Prof. S. Ranganathan [60]. Cocktail effect indicates that the properties of HEAs are certainly related to the properties of its composing elements. The properties can be adjusted easily by selecting the constituent elements and also determining the compositions of the HEAs [61]. Take the

doi:10.6342/NTU202300667

refractory HEAs for example, more and more scholars have paid more attention to refractory HEAs in recent years (e.g., Mo, Nb, Zr, Ta, W, etc.) [62]. With the addition of the refractory metals, the mechanical properties of the HEAs enhance significantly. Furthermore, if more light elements (e.g., Al, Ti etc.) are added to the HEAs, the overall density of the HEAs will be reduced consequently.

2.2 High Entropy Alloy Films (HEAFs)

2.2.1 Magnetron Sputter Deposition of HEAFs

In the magnetron sputtering, the high energy particles bombard the surface of the targets and make the atoms on the target's surface escape and move along a certain direction, consequently films grew on the substrate [63]. Shown in Fig. 2-2, introducing the magnets underneath the target within a vacuum chamber can generate a magnetic field, which is so-called 'magnetron', and the magnetic field can trap the secondary electrons into the discharge and increase Ar's ionization, enhancing the collision rate between the Ar^+ and the surface of the target material [64]. In order to fabricate multi-types of films, several ways such as additional substrate heating or substrate electrical bias can enhance the attraction of charged ions to the substrate with increased kinetic energy. Among all the fabrication processing of the HEAFs, magnetron sputter deposition is the most common technique which is attributed to the three advantages as follow [21, 64]: (i) The deposited films are easy to obtain film stoichiometry similar to the stoichiometry of the

doi:10.6342/NTU202300667

original target even though the different sputter yields among the constituent elements. (ii) A rapid quenching (10^9 K/s) of the magnetron sputter restricts the diffusion of the elements and minimizes the concentration fluctuations in the films. (iii) The films fabricated by magnetron sputter exhibits superior mechanical ability and corrosion-resistances. However, there are also some disadvantages of magnetron sputtering: (i) A slight variation in gas flow rate and working pressure can drastically change the composition of HEAFs. (ii) The sputtering process is time-consuming. (iii) Low target utilization is also a disadvantage of the magnetron sputtering. Moreover, due to the convenience of the incorporation of the reactive gas during sputtering deposition, such as N_2, O_2 etc., the nitride or oxide HEAFs are easily synthesized, providing an effective way to explore more and more HEAFs.

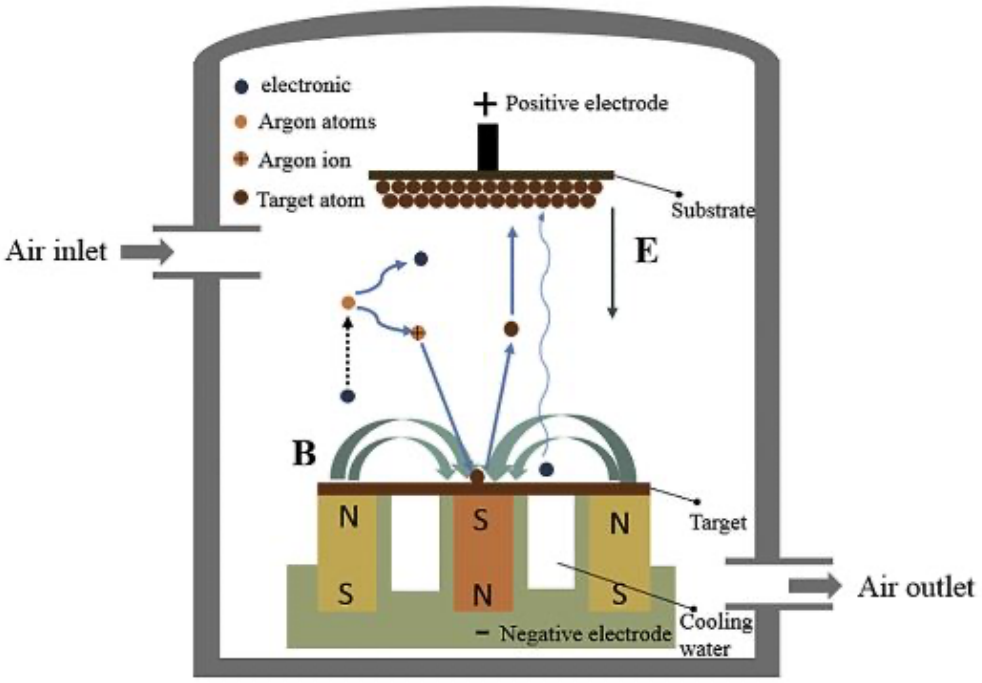

doi:10.6342/NTU202300667

Fig. 2-2 schematic of the magnetron sputtering process [21].

2.2.1 Microstructure and Mechanical properties of HEAFs

High entropy alloy films (HEAFs) have attracted broad interest over the last decade due to their excellent mechanical properties. Compared to bulk HEA materials fabricated by casting, HEAFs fabricated by magnetron sputtering are subjected to the much faster cooling rate that would limit the diffusion of elements and inhibit the grain growth to obtain the much smaller grain sizes. Therefore, scholars put more efforts developing HEAFs in order to meet further requirements to practical applications [5, 6, 8, 26-30, 65-68].

Kim et al. [5] fabricated the NbMoTaW film on Si (100) substrate using direct current (DC) magnetron sputtering and studied the properties of the refractory HEAFs. As shown in Fig. 2-3(a), TEM images indicated that the thickness of the NbMoTaW film was measured to be 350 nm and the BCC structure with a preferential (100) was identified as well. The columnar structure perpendicular to the structure was observed as shown in Fig. 2-3(b). With the high-resolution TEM (HRTEM) image and Inverse FFT (IFFT) results illustrated in Fig. 2-3(c), the calculated average grain size was about 15.1 nm. Besides, the *c*/*a* ratio of the columnar-shape grains was measured to be ~1.8.

doi:10.6342/NTU202300667

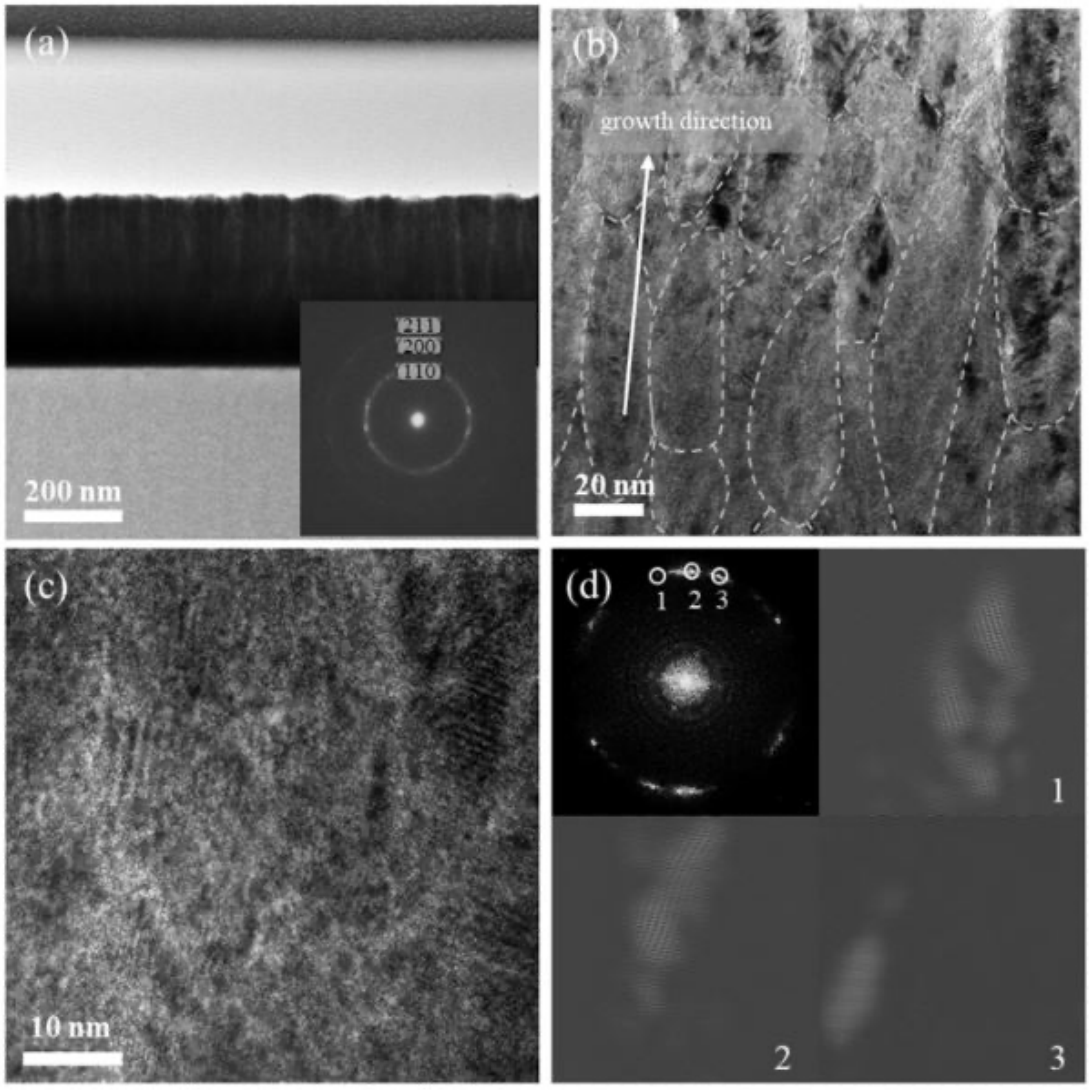

Fig. 2-3 (a, b) Cross-sectional bright-field TEM images of NbMoTaW HEAFs. (c) HRTEM image and (d) FFT pattern (upper left area) of (c) and IFFT image obtained from marked regions in FFT pattern.

Liang et al. [27] studied the effects of Nb addition on microstructures and mechanical properties of CoCrFeMnNi HEAFs. The film without Nb doping exhibited a single FCC phase with strong (111) peak in the XRD spectra shown in Fig. 2-4. As the Nb content increased, the diffraction peak broadened and the other peaks vanished.

doi:10.6342/NTU202300667

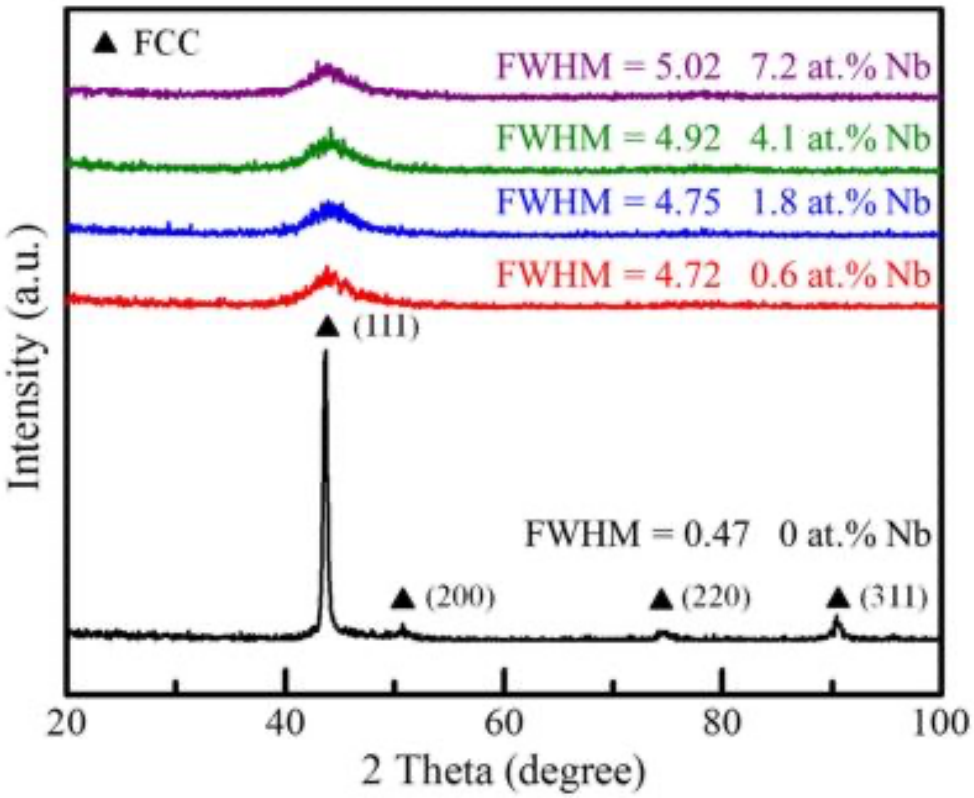

Fig. 2-4 XRD spectra of the $Nb_x(CoCrFeMnNi)_{100-x}$ HEAFs, indicating that the transformation from FCC structure to amorphous phase with the addition of Nb.

The hardness and reduced modulus of the $Nb_x(CoCrFeMnNi)_{100-x}$ HEAFs were presented in Fig. 2-5. The hardness increased from 6.5 to 8.1 GPa as the Nb content increased from 0 to 7.2 at.%, while the reduced modulus decreased with the increasing Nb concentration. The strengthening could be attributed to the grain boundary strengthening and solid solution strengthening. The engineering compressive stress-strain curves of the films subjected to micropillar compression test plotted in Fig. 2-6. indicated that each strain burst in serrated curve which explained a shear band propagation. The yield strength and fracture strength were improved from 1.08 and 2.56 GPa, respectively, for x= 0 to 2.70 and 5.76 GPa, respectively, for x= 7.2. On the other hand, the fracture

doi:10.6342/NTU202300667

strain reduced significantly from 29.4% to 15.8% as the Nb content increased to 7.2 at.% due to the strength-ductility trade-off.

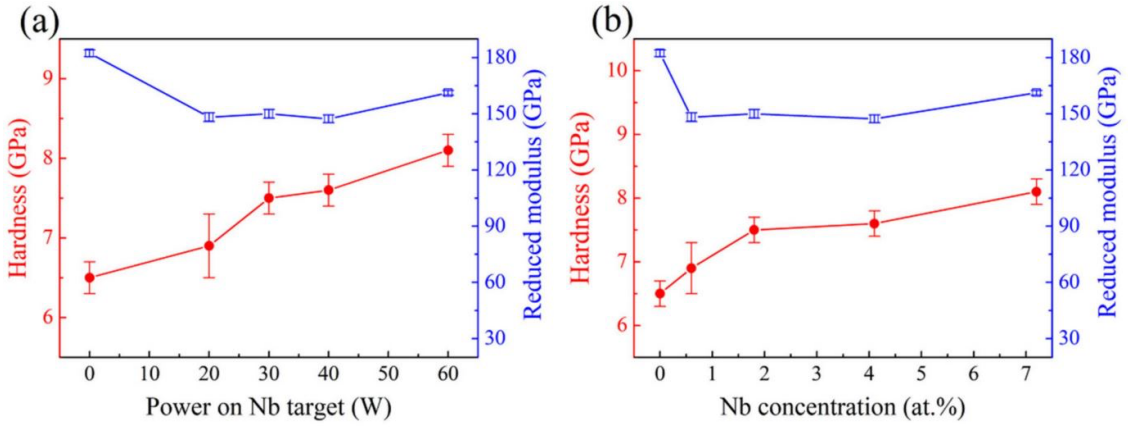

Fig. 2-5 The hardness (H) and reduced Young's modulus (Er) of $Nb_x(CoCrFeMnNi)_{100-x}$ HEAFs as functions of (a) the power applied on Nb target and (b) Nb concentration.

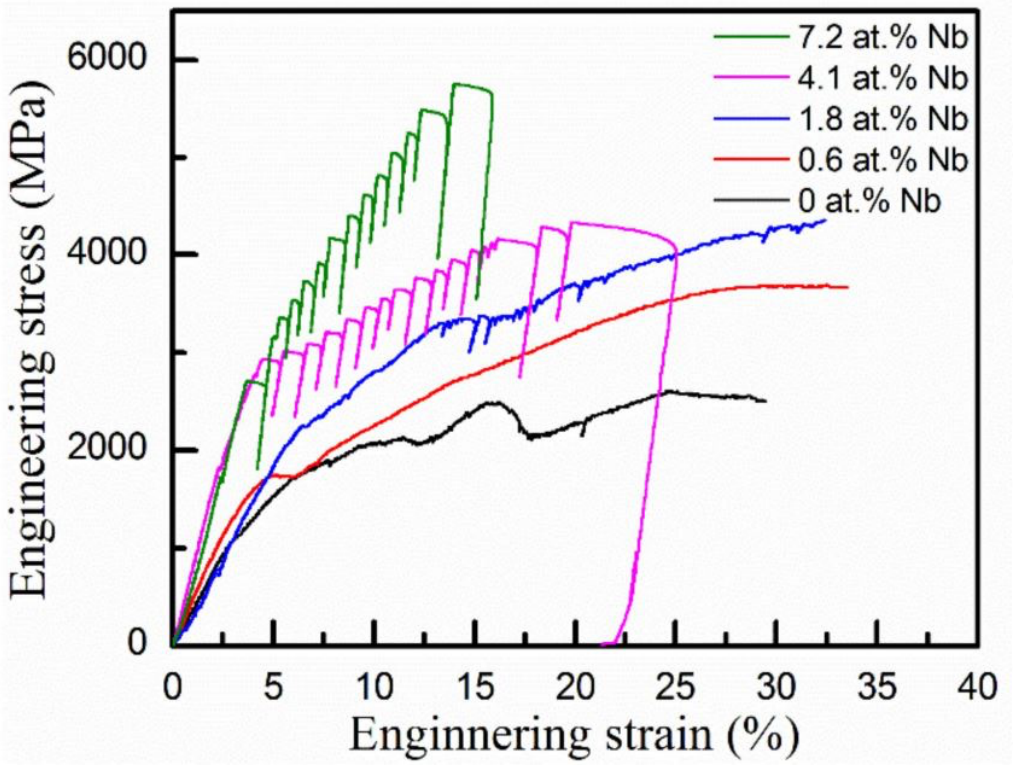

Fig. 2-6 Engineering compressive stress–strain curves of micropillar compression tests of $Nb_x(CoCrFeMnNi)_{100-x}$ HEAFs.

doi:10.6342/NTU202300667

2.3 Introduction of High Entropy Alloy Nitride Films (HEANFs)

2.3.1 Microstructure and Mechanical properties of HEANFs

Since the 2010s, high-entropy alloy nitride films (HEANFs) have received much attention due to their superior mechanical properties, such as high hardness [14, 18], excellent electrical properties [15], corrosion resistances [16] and creep behaviors [17]. Those excellent mechanical properties are attributed to the formation of strong mixed ion-metal-covalent bonds. Moreover, nitrides could serve as the heterogeneous nucleation sites for crystallization and thus the structure of HEANFs presented in existing works mostly exhibited highly crystallized grains. Cui et al. [18] prepared the (AlCrTiZrHf)N films using radio frequency (RF) magnetron sputtering with different N_2 flow rates. As the nitrogen content increased from 0 to ~50 at.%, the hardness was improved from 17.9 to 33.1 GPa shown in Fig. 2-7. Fig. 2-8 shows the sputtering rate of (AlCrTiZrHf)N HEANFs as functions of gas flow ratio of N_2/Ar. The sputtering rate decreased from 25.57 to 8.02 nm/min with the nitrogen addition. The phenomenon is so-called target poisoning [7, 69].

doi:10.6342/NTU202300667

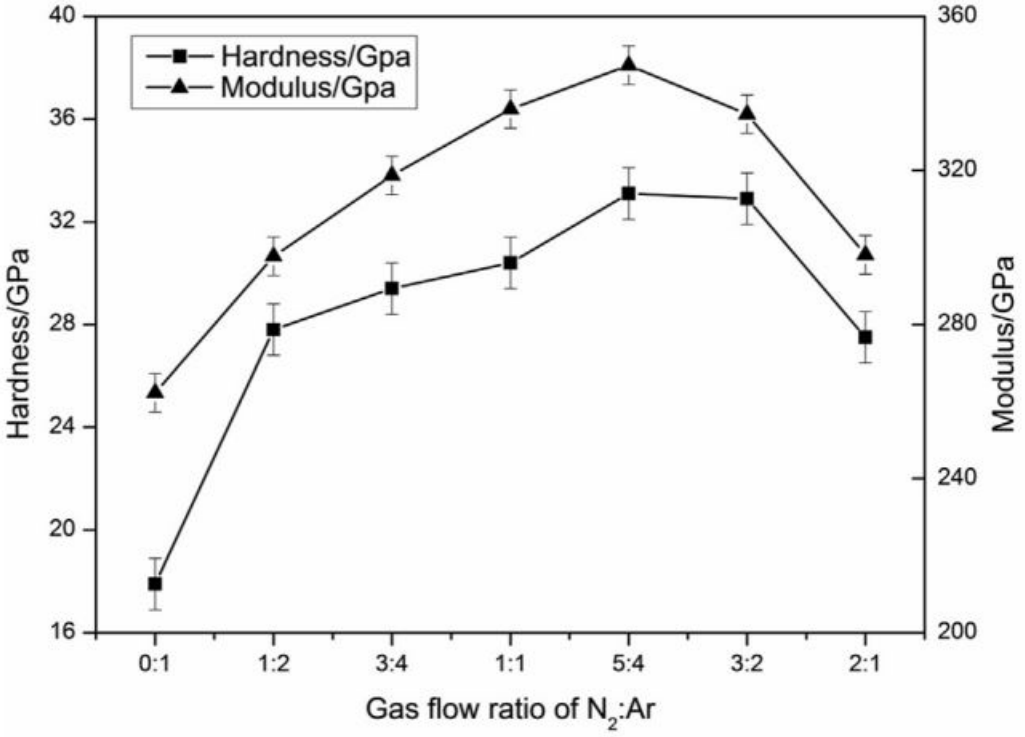

Fig. 2-7 Hardness and elastic modulus of (AlCrTiZrHf)N HEANFs with different N_2 flow rates.

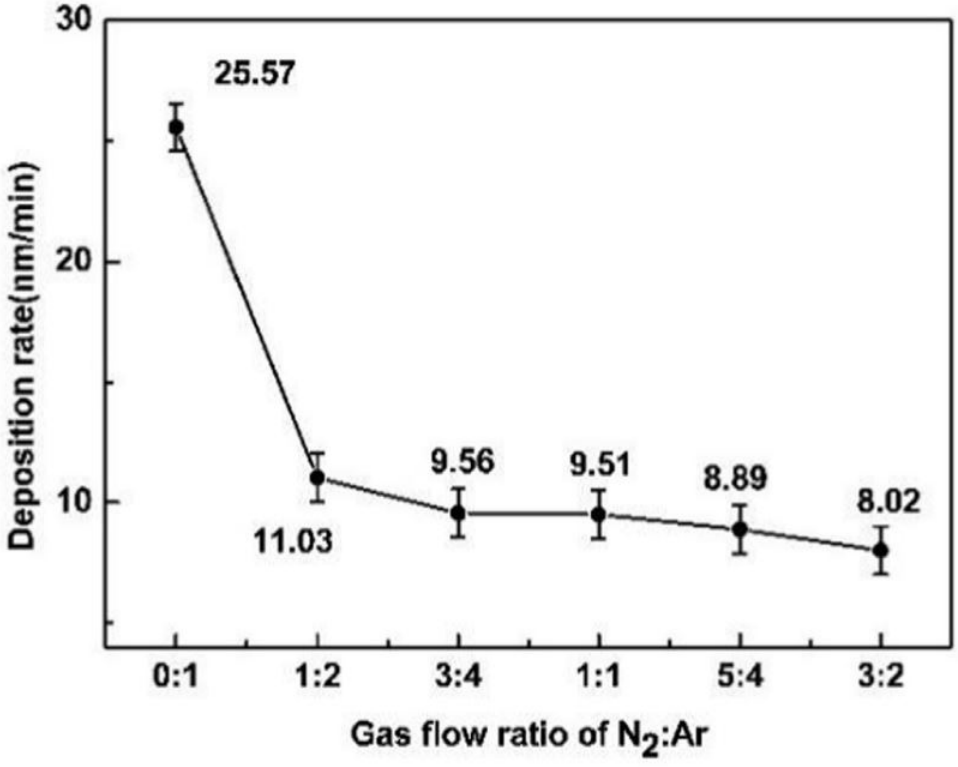

Fig. 2-8 Sputtering rate of (AlCrTiZrHf)N HEANFs as functions of N_2/Ar flow ratio.

Chang et al. [24] deposited TiVCrAlZr HEANFs by reactive magnetron sputtering on

doi:10.6342/NTU202300667

silicon (100) wafers and found that the TiVCrAlZr film exhibited an amorphous phase illustrated in Fig. 2-9. With the increase of nitrogen flow rate, the crystallization was enhanced and presented NaCl-type FCC structure. Fig. 2-10 illustrates the SEM morphologies of TiVCrAlZr HEANFs and suggests with the addition of nitrogen, the triangular grains were found due to the surface energy minimization. When the N_2 flow rate is above 16.7%, domed clusters were found.

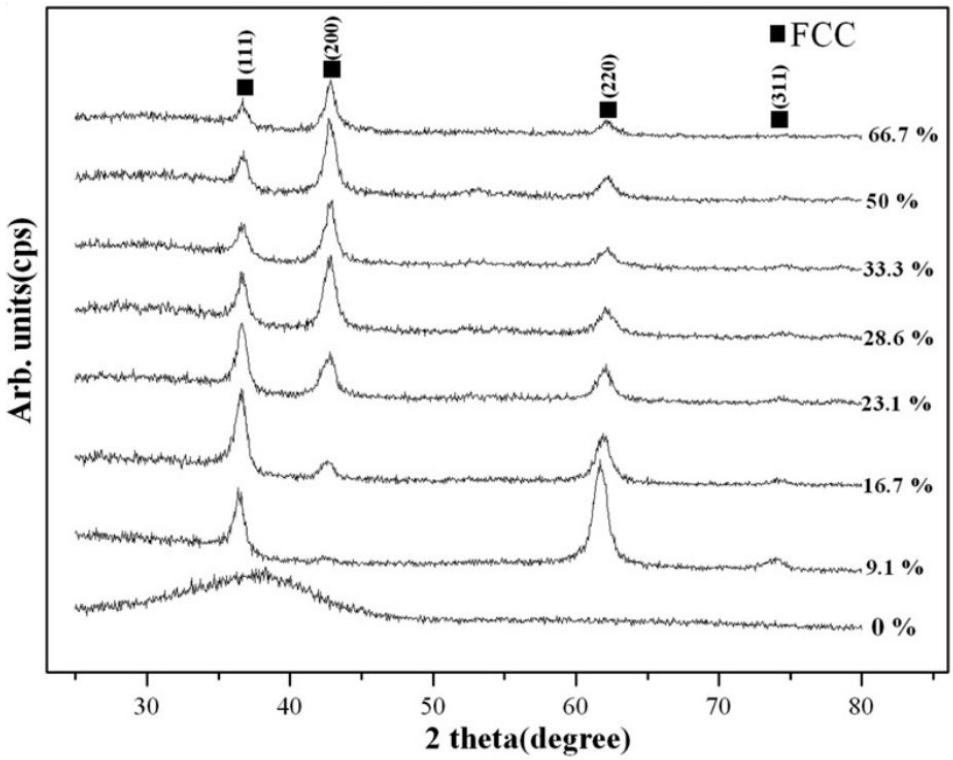

Fig. 2-9 XRD spectra of multi-element TiVCrAlZr HEANFs deposited under different RN, showing a (220) preferential orientation at R_N = 9.1%, a (111) preferential orientation at R_N = 16.7% and a (200) preferential orientation at R_N = 50%.

doi:10.6342/NTU202300667

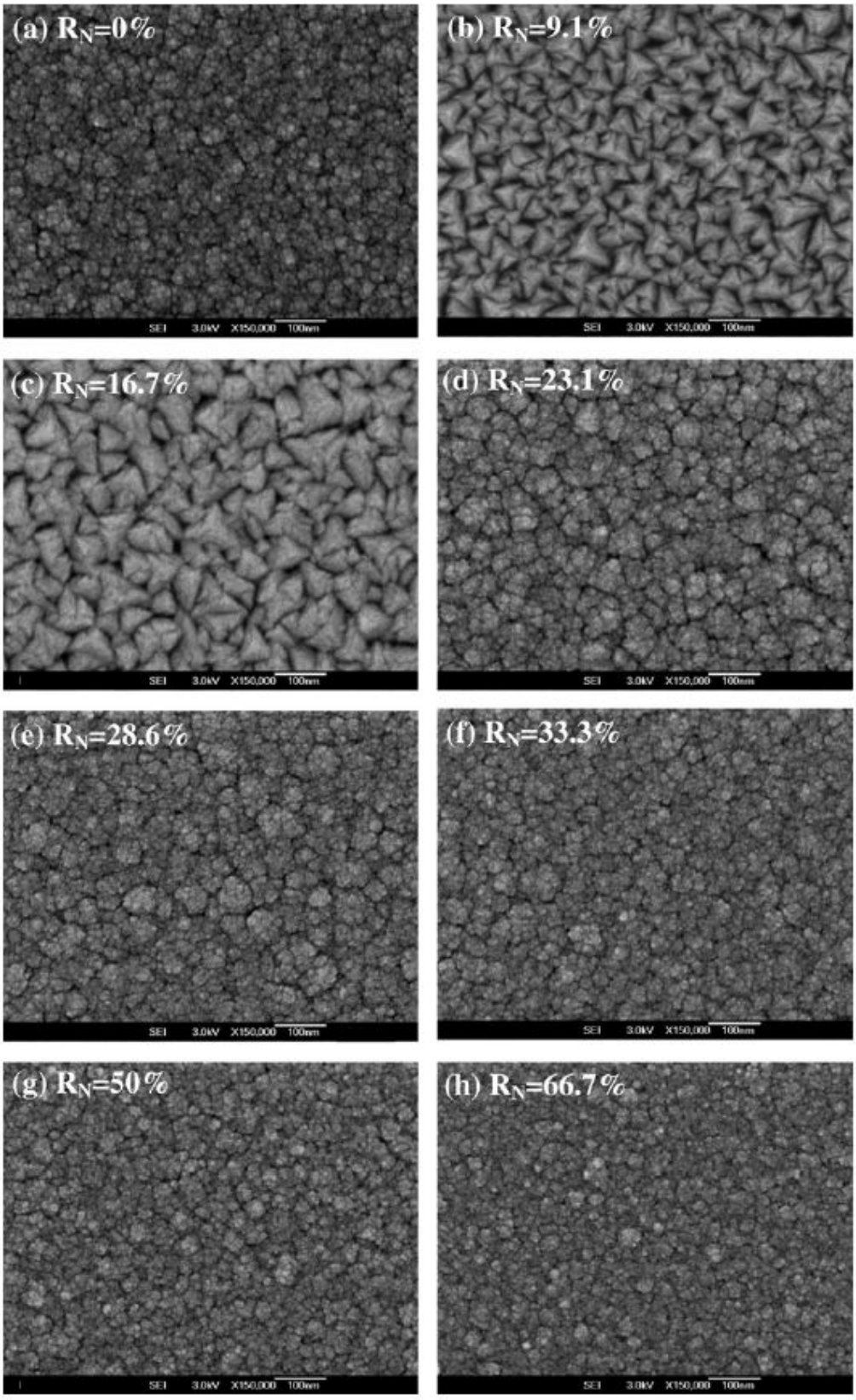

Fig. 2-10 SEM plane-view morphology of multi-element TiVCrAlZr HEANFs deposited under different N_2 flow ratios.

In the SEM images, the typical columnar microstructures were clearly characterized

doi:10.6342/NTU202300667

in each film with different R_N flow rates plotted in Fig. 2-11. The hardness and modulus of the TiVCrAlZr HEANFs with different N_2 flow rates as a function of R_N were obtained and shown in Fig. 2-12. With the addition of nitrogen, the hardness of the TiVCrAlZr HEANFs increased from 8.2 to 11.0 GPa and the elastic modulus increased from 128.9 to 152 GPa. The enhancement of the mechanical properties could be attributed to the formation of mixed ion-metal-covalent bonds.

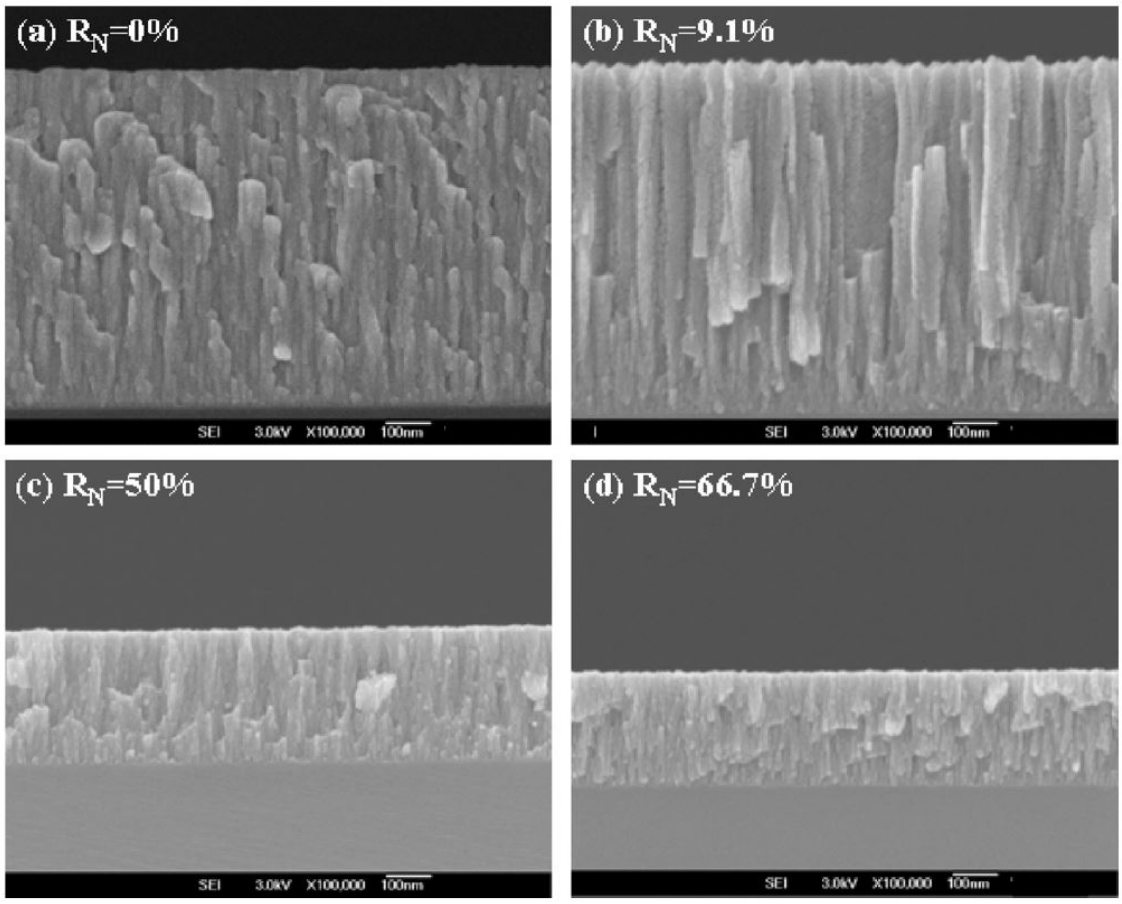

Fig. 2-11 SEM cross-sectional morphology of multi-element TiVCrAlZr HEANFs deposited under different N_2 flow ratios.

doi:10.6342/NTU202300667

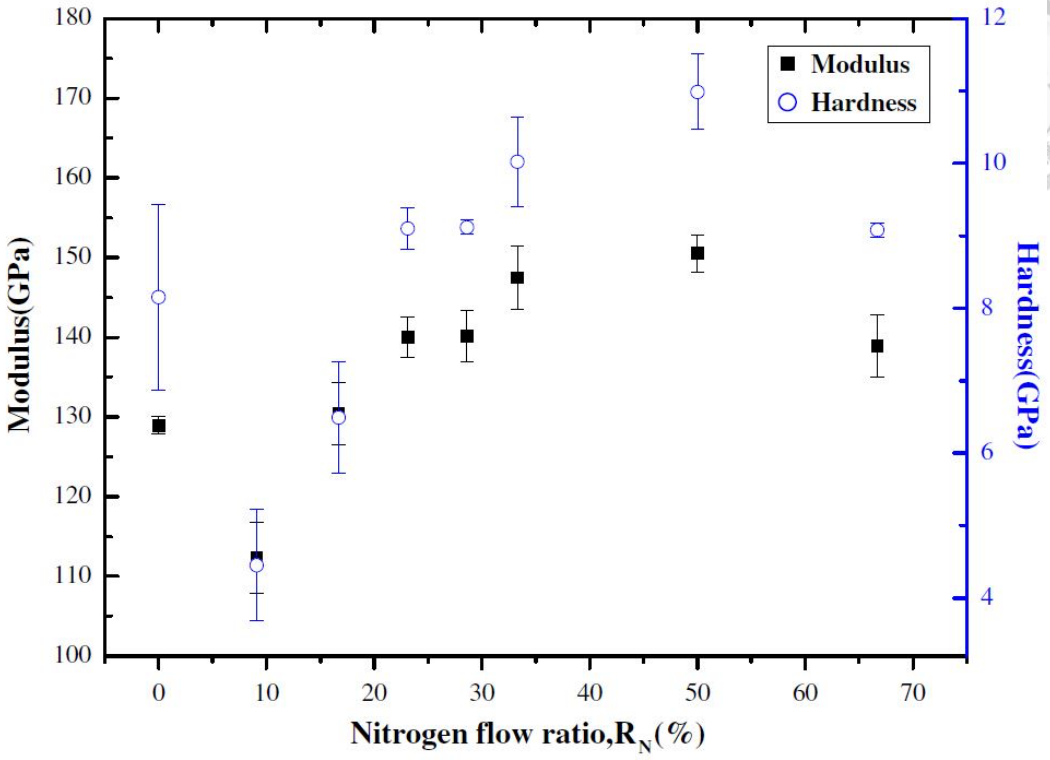

Fig. 2-12 Hardness and modulus of multi-element TiVCrAlZr HEANFs deposited under different R_N flow rates.

2.4 Effect of Alloy Addition

In recent years, various studies have proven that doping certain elements into HEAs can effectively influence the microstructures and improve the mechanical properties significantly (e.g., Mo, V, and Ce etc.) [26-30]. Hence, the effects of alloy addition to HEAs on the microstructures and mechanical properties have been investigated which will be introduced in this section.

2.4.1 Mo Addition in HEAFs

In 2021, Huang et al. [28] reported the effects of the Mo addition to the CoCrFeMnNi HEAFs on the microstructures and mechanical properties. Fig. 2-13 shows that with the addition of Mo, the peak at 43.6º in each film was broadened significantly, indicating the

doi:10.6342/NTU202300667

decreasing crystallinity. Moreover, the $Mo_{0.5}$ and $Mo_{1.0}$ films were found to be asymmetric. Through the further investigation with slower scan rate, the presence of HCP phase was identified in both the $Mo_{0.5}$ and $Mo_{1.0}$ films.

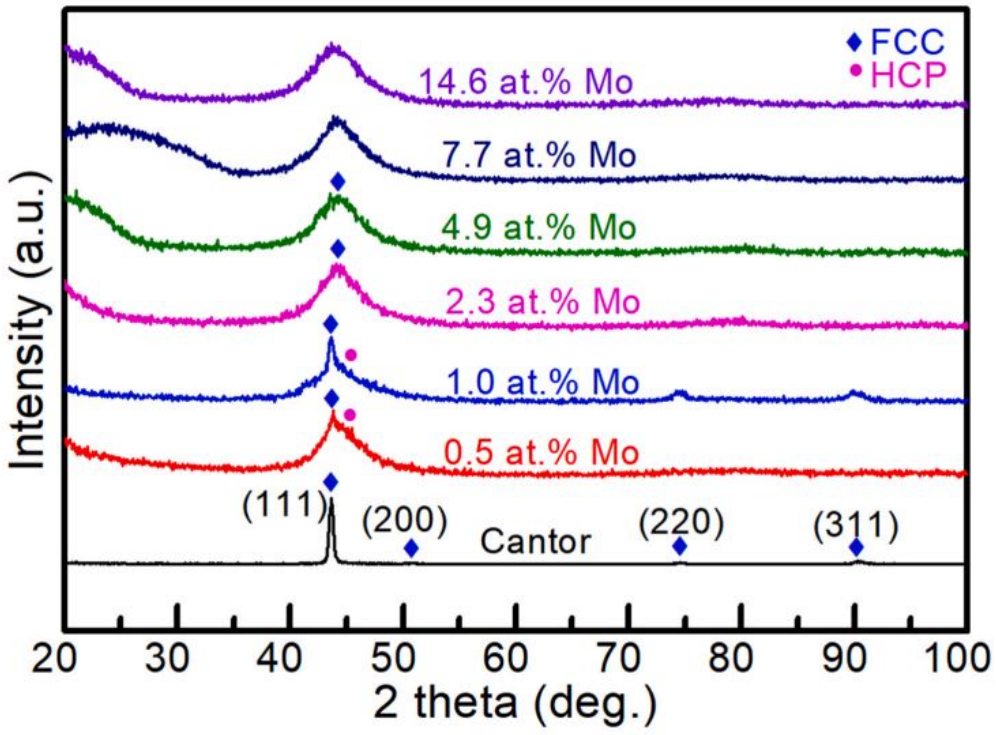

Fig. 2-13 XRD spectra of the $(CoCrFeMnNi)_{100-x}Mo_x$ HEAFs with different Mo contents.

Nano-scratch tests were conducted to determine the load bearing capacity of the film subjected to both normal and tangential forces, and the coefficient of friction (COF) of the film could be obtained by dividing the lateral tangential force by the normal force. The variations of COF with scratch distance of three films under a constant load of 10 μN shown in Fig. 2-14. The results showed that the $Mo_{14.6}$ film exhibited the lowest COF value. The results proved that the tribological properties of the $(CoCrFeMnNi)_{100-x}Mo_x$ HEAFs could be effectively improved with the increasing Mo concentration.

doi:10.6342/NTU202300667

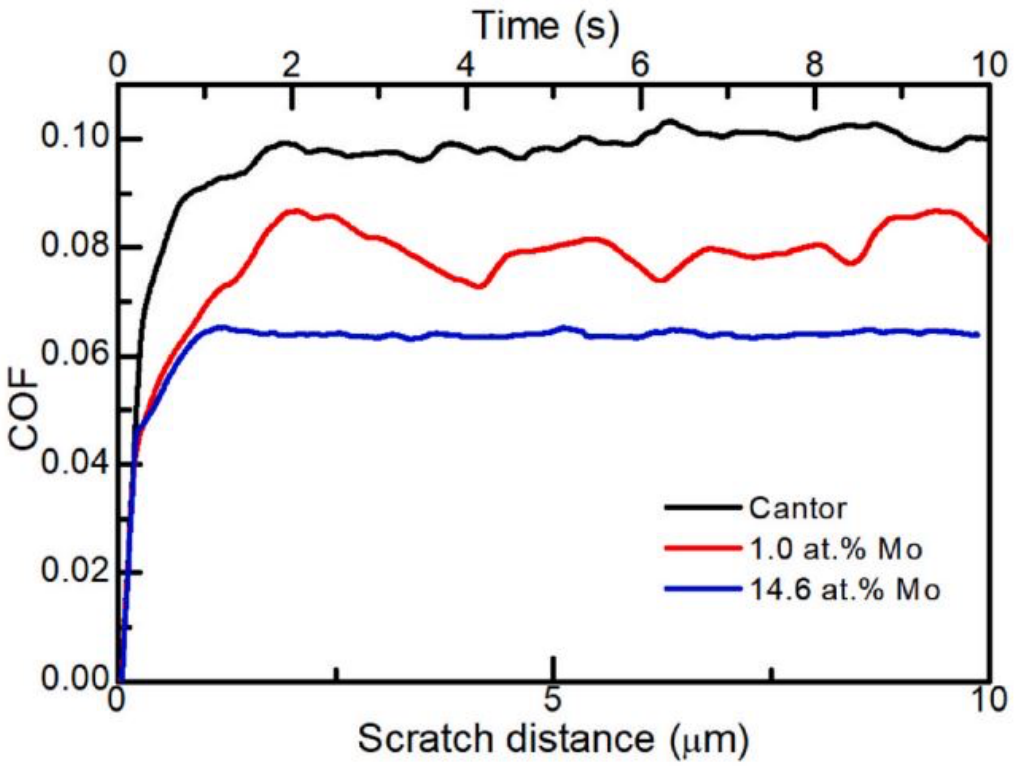

Fig. 2-14 The variation of COF as a function of scratch distance for Mo_0, $Mo_{1.0}$ and $Mo_{14.6}$ film, respectively.

2.4.2 Ce Addition in medium entropy alloy films (MEAFs)

Lin et al. [26] deposited the $(CoCrNi)_{100-x}Ce_x$ MEAFs on Si(100) substrates using RF magnetron co-sputtering of CoCrNi alloy target and Ce target. The cross-sectional bright field (BF) TEM images and corresponding selected area electron diffraction (SAED) patterns shown in Fig. 2-15 revealed that for the BF images of Ce_0 and $Ce_{1.05}$ films, the columnar structure with the planar defects was identified and the films showed the FCC structure with the corresponding SAED results. With the further addition of Ce content at 4.2 at.%, the $(CoCrNi)_{100-x}Ce_x$ MEAFs exhibited the structure contained nanocrystalline grains embedded in an amorphous structure.

doi:10.6342/NTU202300667

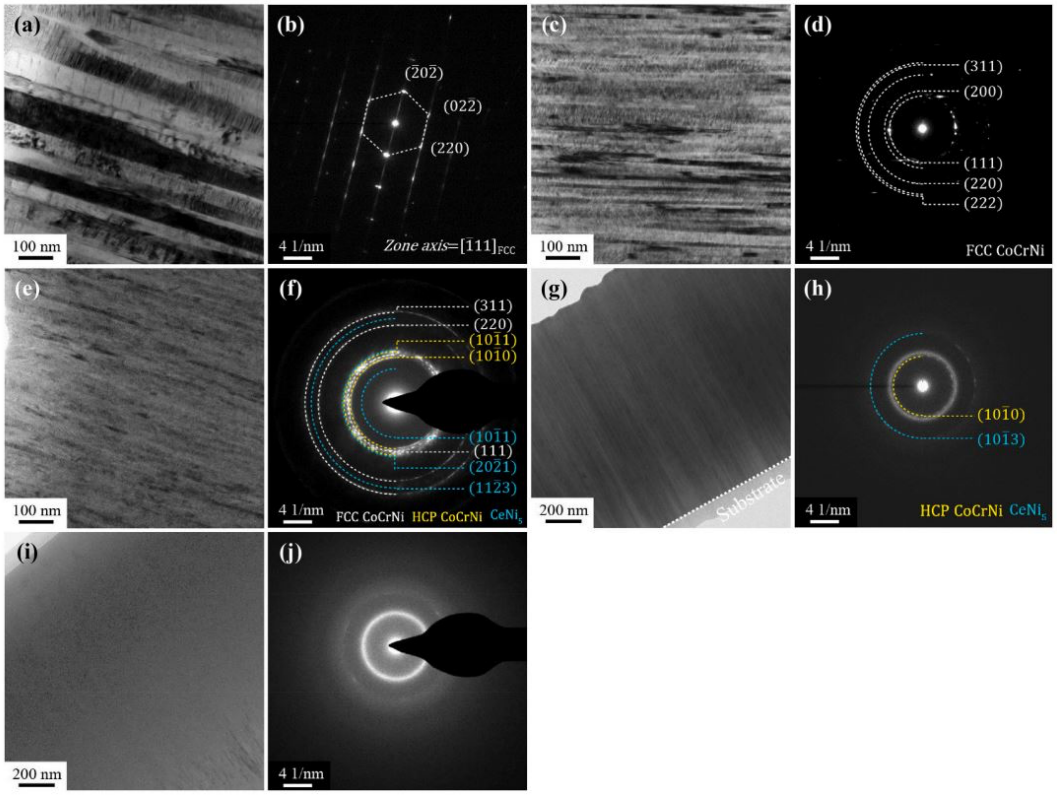

Fig. 2-15 The TEM images and the corresponding SAED patterns. (a, b) Ce_0, (c, d) $Ce_{1.05}$, (e, f) $Ce_{2.61}$, (g, h) $Ce_{4.2}$, and (i, j) $Ce_{5.96}$ films.

The SEM images of the deformed micropillars after compression tests are illustrated in Fig. 2-16. No apparent shear banding could be found for Ce_0, $Ce_{1.05}$, $Ce_{2.61}$ films shown in Fig. 2-16(a), (b) and (c), respectively, while the shear bands were observed in Fig. 2-16(d) and (e) for $Ce_{4.2}$ and $Ce_{5.96}$ films. The SEM results of the deformed micropillars were consistent to the formation of amorphous phases in Fig. 2-15.

doi:10.6342/NTU202300667

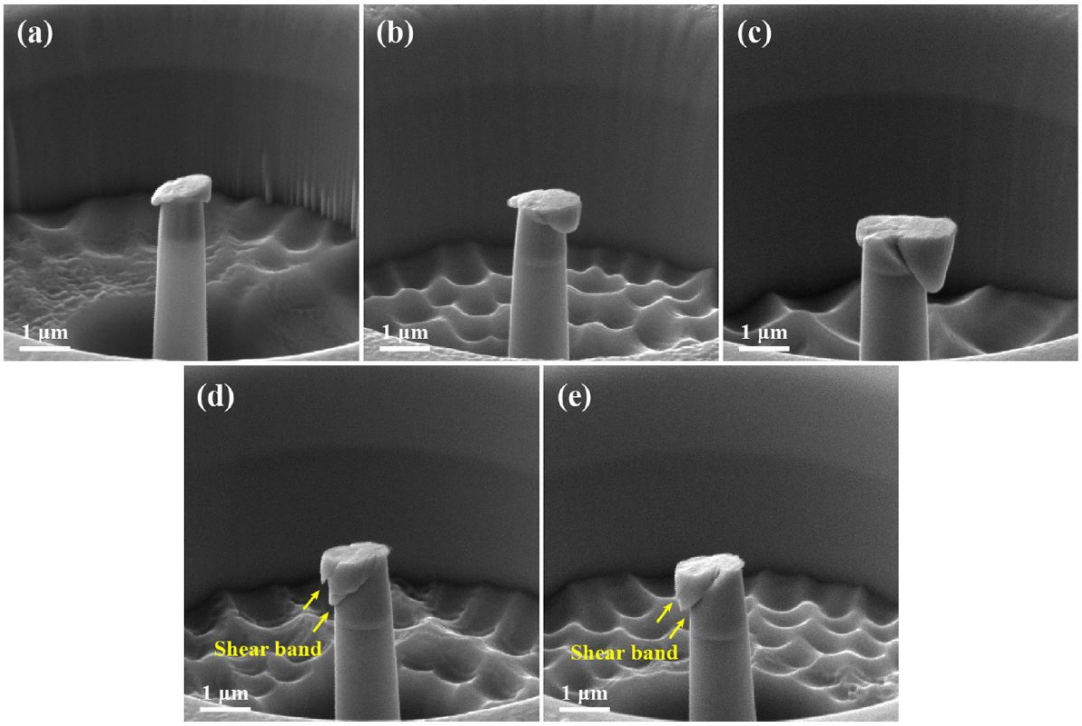

Fig. 2-16 The SEM images of the deformed micropillars after compression tests for (a) Ce_0, (b) $Ce_{1.05}$, (c) $Ce_{2.61}$, (d) $Ce_{4.2}$ and (e) $Ce_{5.96}$ film.

2.5 Effects of Al Addition

2.5.1 Al Addition in Bulk NbTiVZr system

Xu et al. [31] and Stepanov et al. [32] independently introduced Al to the NbTiVZr alloy system since Al has a negative mixing enthalpy with the constituent elements in NbTiVZr alloy (the mixing enthalpies of Al with Nb, Ti, V and Zr atomic pairs are -18, -30, -16, and -44 kJ/mol, respectively). Moreover, the increasing Al concentration decreased the difference in alloy atomic size which stabilized the solid solution structure but also increased the system's mixing enthalpy at the same time, making it easier for Al-attractive elements to form the second phase.

With the addition of Al, the C14 Laves phase was identified in BCC matrix phase.

doi:10.6342/NTU202300667

The second phase began to precipitate along the grain boundaries, and some of the second phase existed in the interdendritic region of matrix separately.

Without Al addition, the NbTiVZr alloy exhibited the peak stress of 1470 MPa but a poor plastic strain of 4.2% [31]. However, the incorporation of Al in the NbTiVZr alloy successfully helped the $Al_{0.3}$NbTiVZr alloy to possess a higher yield strength of 1367 MPa and superior compressive ductility of 10.14%.

2.5.2 Al Addition in HEAFs

Feng et al. [35] fabricated the Al_xCoCrFeNi HEAFs and found that with the Al addition, the structure changed from FCC to BCC and the hardness increased from 3.8 to 4.3 GPa. Hsu et al. [34] fabricated the Al_xCoCrFeMnNi HEAFs using RF magnetron sputtering system by co-sputtering of CoCrFeMnNi alloy and Al targets and studied the effects of Al doping on the microstructure and mechanical properties of CoCrFeMnNi HEAFs. With the scan rate of 4º/min, the XRD patterns of Al_xCoCrFeNi HEAFs with different Al contents are shown in Fig. 2-17. For Al_0 and $Al_{0.7}$ films, the XRD patterns showed single FCC phase without the presence of any precipitates. However, with the further addition of Al, the $(110)_{BCC}$ diffraction peak appeared and suggested the formation of a new crystalline structure of BCC.

In order to acquire a better resolution for $Al_{0.3}$ and $Al_{0.6}$ films, the slower scan rate of 1º/min was performed from 40º and 50º and the corresponding XRD patterns are shown

doi:10.6342/NTU202300667

in Fig. 2-18(a). Moreover, the deconvoluted pattern of $Al_{0.6}$ is presented in Fig. 2-18(b). The results with slow scan confirmed the transformation of structure shown in Fig. 2-17.

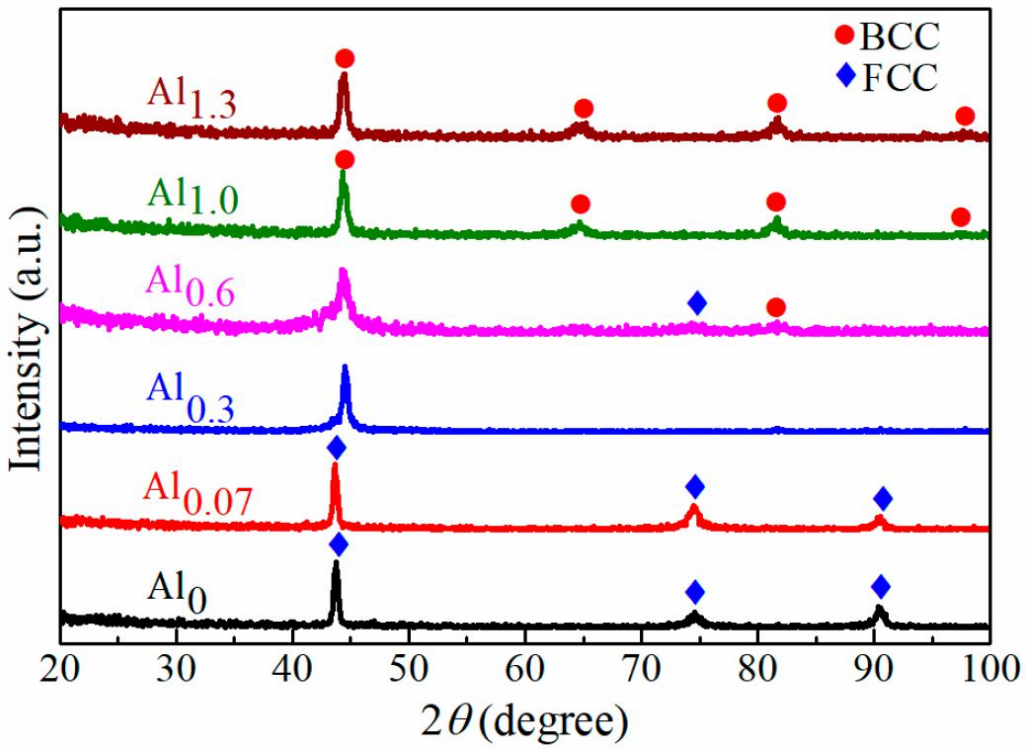

Fig. 2-17 XRD patterns of $CoCrFeMnNiAl_x$ HEAFs with the scan rate of 4°/min.

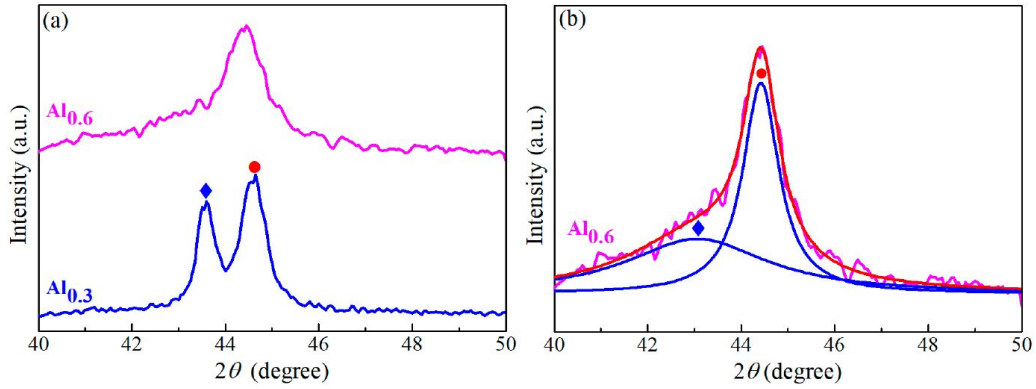

Fig. 2-18 (a) XRD patterns of Al0.3 and Al0.6 films using a slower scan rate of 1°/min and (b) the deconvoluted pattern for Al0.6 film from (a).

The compressive stress-strain curves of $Al_xCoCrFeNi$ HEAFs are illustrated in Fig. 2-19. A load drop was found in $Al_{0.07}$, $Al_{0.3}$ and $Al_{0.6}$ films in the presence of the FCC structure but not in $Al_{1.0}$ and $Al_{1.3}$ films, which had BCC structure. As a result, the addition

doi:10.6342/NTU202300667

of Al to the CoCrFeMnNi HEAFs could effectively enhance the strength shown in Fig. 2-19.

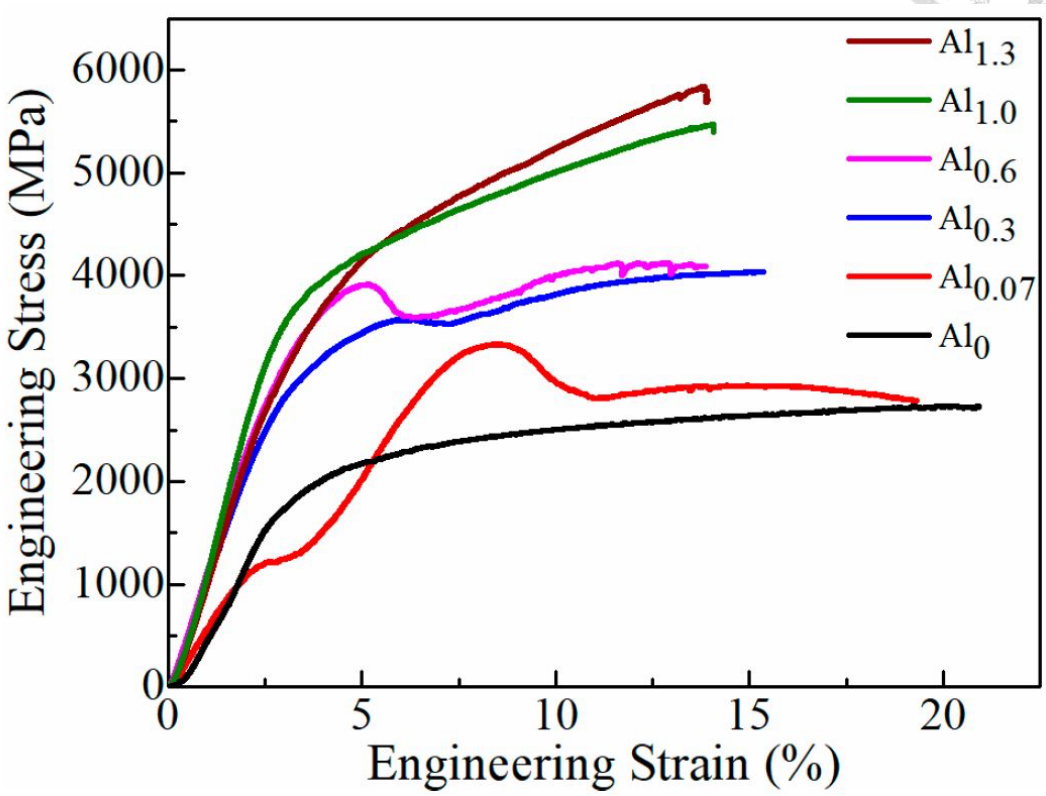

Fig. 2-19 The compressive engineering stress−strain curves of the CoCrFeMnNiAl_x HEAFs.

doi:10.6342/NTU202300667

Chapter 3 Experimental Procedures

3.1 Experimental Flow

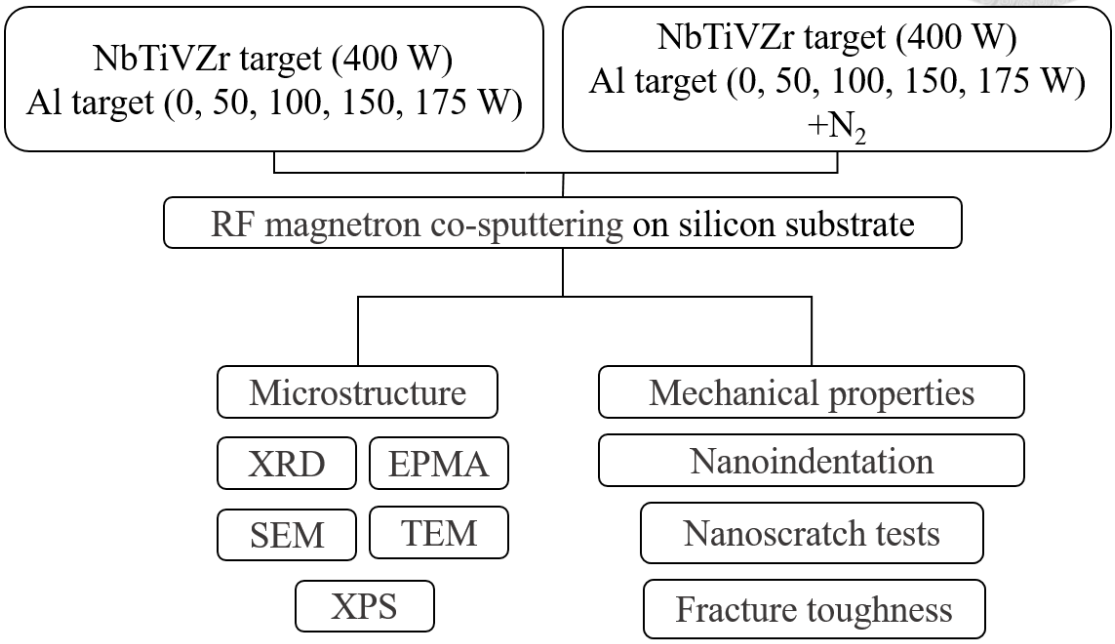

Fig. 3-1 The flow charts of the experimental procedures of the $(NbTiVZr)_{100-x}Al_x$ HEAFs and $(NbTiVZrN)_{100-x}Al_x$ HEANFs.

3.2 Sample preparations and Deposition Process

3.2.1 $(NbTiVZr)_{100-x}Al_x$ HEAFs

The $(NbTiVZr)_{100-x}Al_x$ HEAFs were deposited on silicon (100) substrates by radio frequency (RF) magnetron co-sputtering of NbTiVZr alloy (purity >99.99 wt.%) and Al (purity >99.99 wt.%) targets. Both targets were manufactured with the diameter of 76.2 mm and thickness of 6 mm. Before the film deposition, all of the substrates were ultrasonically cleaned and rinsed with acetone, ethanol and deionized water sequentially for 15 min in each step. The working distance between NbTiVZr alloy target and substrate was fixed at 10 cm, and the substrate-to-Al target distance was 20 cm. Prior to the film

doi:10.6342/NTU202300667

deposition, the chamber was first evacuated to a vacuum better than 1.3×10^{-4} Torr at room temperature, and the two targets were respectively cleaned by argon ion bombardment for 30 min in order to remove the contamination and oxide on the surface. During sputtering, the power of NbTiVZr target was fixed at 400 W and the power applied on the Al target was regulated at 0, 50, 100, 150, 175 W, respectively, to control the Al content in the films. The Ar flow rates were maintained at 20 sccm. The working pressure was kept at 0.4 Pa and the substrate rotated at a rate of 30 rpm to ensure the uniformity of the films. All deposition procedures were conducted for 50 min at room temperature without substrate bias.

3.2.2 $(NbTiVZrN)_{100-x}Al_x$ HEANFs

The $(NbTiVZrN)_{100-x}Al_x$ HEANFs were deposited on silicon (100) substrates by radio frequency (RF) magnetron co-sputtering of NbTiVZr alloy (purity >99.99 wt.%) and Al (purity >99.99 wt.%) targets. Both targets were manufactured with the diameter of 76.2 mm and thickness of 6 mm. Before the film deposition, all of the substrates were ultrasonically cleaned and rinsed with acetone, ethanol and deionized water sequentially for 15 min in each step. The working distance between NbTiVZr alloy target and substrate was fixed at 10 cm, and the substrate-to-Al target distance was 20 cm. Prior to the film deposition, the chamber was first evacuated to a vacuum better than 1.3×10^{-4} Torr at room temperature, and the two targets were respectively cleaned by argon ion bombardment for

doi:10.6342/NTU202300667

30 min in order to remove the contamination and oxide on the surface. During sputtering, the power of NbTiVZr target was fixed at 400 W and the power applied on the Al target was regulated at 0, 50, 100, 150, 175 W, respectively, to control the Al content in the films. The Ar and N_2 flow rates were maintained at 15 and 5 sccm, respectively. The working pressure was kept at 0.4 Pa and the substrate rotated at a rate of 30 rpm to ensure the uniformity of the films. All deposition procedures were conducted for 50 min at room temperature without substrate bias.

3.3 Analytical Techniques

3.3.1 Electron Probe X-ray Microanalyzer (EPMA)

The compositions of the films were determined by the electron probe X-ray microanalyzer (EPMA, JEOL JXA-8530F PUS, Japan). Five points were selected randomly from each specimen with the spot size of 30 μm to measure the overall constituent composition in the alloys to check the uniformity of the HEAFs.

3.3.2 X-ray Diffraction (XRD)

The crystalline structure of the films was detected by X-ray diffractometer (XRD, Rigaku TTRAX 3, Japan) with Cu Kα (λ =0.154606 nm). The grazing-incidence angle of 0.9 º was determined before scanning to prevent the diffraction from the Si substrate. The samples were scanned in the 2θ range from 20º to 80º at a scan rate of 4º/min.

doi:10.6342/NTU202300667

3.3.3 SEM Observation

The surface morphology and film thickness of the films were determined by a field-emission scanning electron microscope (SEM, NOVA NANO SEM 450, FEI, Hillsboro, OR, USA) with an acceleration voltage of 10 kV.

3.3.4 TEM Observation

Transmission electron microscopy (TEM, FEI Tecnai G2 F20, Hillsboro, OR, USA) was used to further study the detailed microstructure and crystallinity of the films. The high-resolution TEM (HRTEM) images for further investigation were analyzed by Gatan Digital Micrograph software. TEM specimens of the films were prepared by a dual-beam focused ion beam system (FIB, FEI Versa 3D, USA).

3.3.5 XPS analysis

The chemical bonding characteristics of the films was evaluated by X-ray photoelectron spectroscopy (XPS, PHI 3000 VersaProbe III) with Al Kα irradiation at a pass energy of 1486.6 eV. Before the XPS measurement, the surface contaminants on the films were removed by Ar^+ ion beam at a primary energy of 3 keV for 5 min.

3.3.6 Nanoindentation tests

Hardness and reduced modulus were acquired using the nanoindenter (Hysitron TI 950 TriboIndenter, Bruker, USA) with the Berkovich indenter tip having a tip radius of 150 nm. In order to avoid the substrate effect, the penetration depth was controlled at 80

doi:10.6342/NTU202300667

nm while the film thicknesses were in the range of 1.19 to 1.45 μm. At least ten indentations were performed for each test to avoid data deviation.

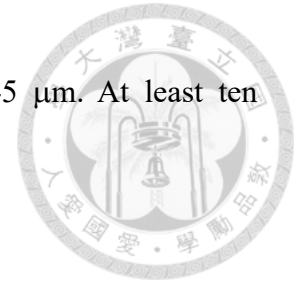

3.3.7 Fracture toughness tests

Fracture toughness (K_{IC}) is another vital mechanical property of films and it was widely evaluated from indentation-induced radial cracking method, which was initially proposed for bulk materials. This method was usually conducted on brittle materials with sharp indenters, such as Vickers and Berkovich indenters, and the nanoindentation tests with Berkovich tip was adopted to evaluate the fracture toughness in this work. The relationship between the fracture toughness and the length of radial cracks was calculated by the following equation [70, 71]:

$$K_{1C} = \alpha(\frac{E}{H})^{\frac{1}{2}}(\frac{P}{c^{3/2}}) \quad (5)$$

where E and H are the elastic modulus and hardness of the films, respectively, P is the peak indentation load, c is the crack length, and α is the empirical constant which depends on the geometry of the indenter, and α=0.016 for both the Berkovich and Vickers type indenters. The cracks captured by optical microscope were presented in Fig. 3-2. The values of fracture toughness were acquired using the nanoindenter (Hysitron TI 950 TriboIndenter, Bruker, USA) with the Berkovich indenter tip. The load was controlled at 10000 μN and the penetration depth was about 120 nm. The images were scanned at the scan rate of 0.5 Hz. At least twenty indentations were performed for

doi:10.6342/NTU202300667

each test to avoid data deviation.

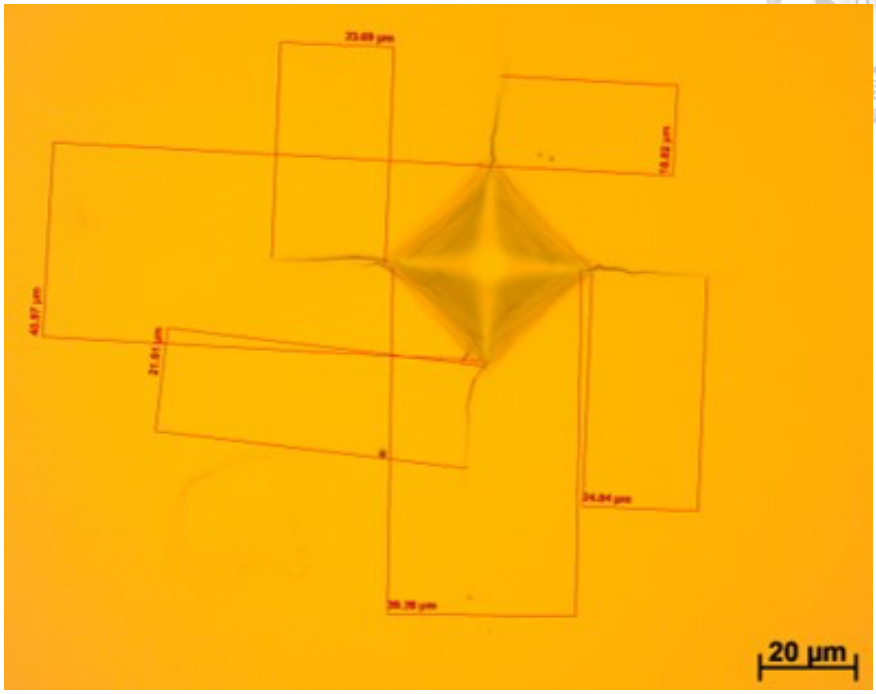

Fig. 3-2 the optical microscope images of the indent with the Vickers hardness testers.

3.3.8 Nanoscratch tests

The values of coefficient of friction (COF) of $(NbTiVZrN)_{100-x}Al_x$ HEAFs were measured with the nanoscratch tests using the nanoindenter (Hysitron TI 950 TrinoIndenter, Bruker, USA) equipped with a conical tip of 5 μm radius. The normal load of the scratch tests was ramped from 0 to 5000 μN with the loading rate of ~417 μN/s, and the scratch length was fixed at 10 μm. Four scratch tests were conducted on each film.

Chapter 4 Results and Discussion

4.1 $(NbTiVZr)_{100-x}Al_x$ HEAFs

4.1.1 Chemical Compositions

The chemical compositions of the $(NbTiVZr)_{100-x}Al_x$ HEAFs analyzed by EPMA are

doi:10.6342/NTU202300667

presented in Table 4-1. The content of Al increased from 3.5 to 12.9 at.% as the power applied on Al target increased from 50 W to 175 W. The concentrations of Nb, Ti, V, Zr were nearly equimolar and the slightly deviation could be attributed to the different sputtering yields of each element. For convenience, the $(NbTiVZr)_{100-x}Al_x$ HEAFs were donated as Al_x film in the 4.1 section.

Table 4-1 The chemical compositions of $(NbTiVZr)_{100-x}Al_x$ HEAFs with different powers applied on Al target.

Power	*x*	Nb	Ti	V	Zr	Al
0	0	22.89±0.05	27.84±0.15	24.77±0.22	24.45±0.11	0.00±0.00
50	3.5	22.29±0.06	26.91±0.19	23.87±0.15	23.44±0.11	3.48±0.02
100	7.3	21.36±0.11	25.98±0.25	22.67±0.57	22.62±0.15	7.35±0.06
150	12.2	19.78±0.41	24.66±0.08	21.82±0.33	21.49±0.10	12.24±0.02
175	12.9	20.04±0.18	23.34±0.69	20.19±0.23	23.51±0.28	12.91±0.15

4.1.2 XRD Results

From the XRD patterns shown in Fig. 4-1, it can be seen that all the $(NbTiVZr)_{100-x}Al_x$ HEAFs with different Al content present a single low-intensity wide peak. The results indicated all the films exhibit amorphous phase. The strong amorphization of the $(NbTiVZr)_{100-x}Al_x$ HEAFs inhibited the grain growth effectively [72].

doi:10.6342/NTU202300667

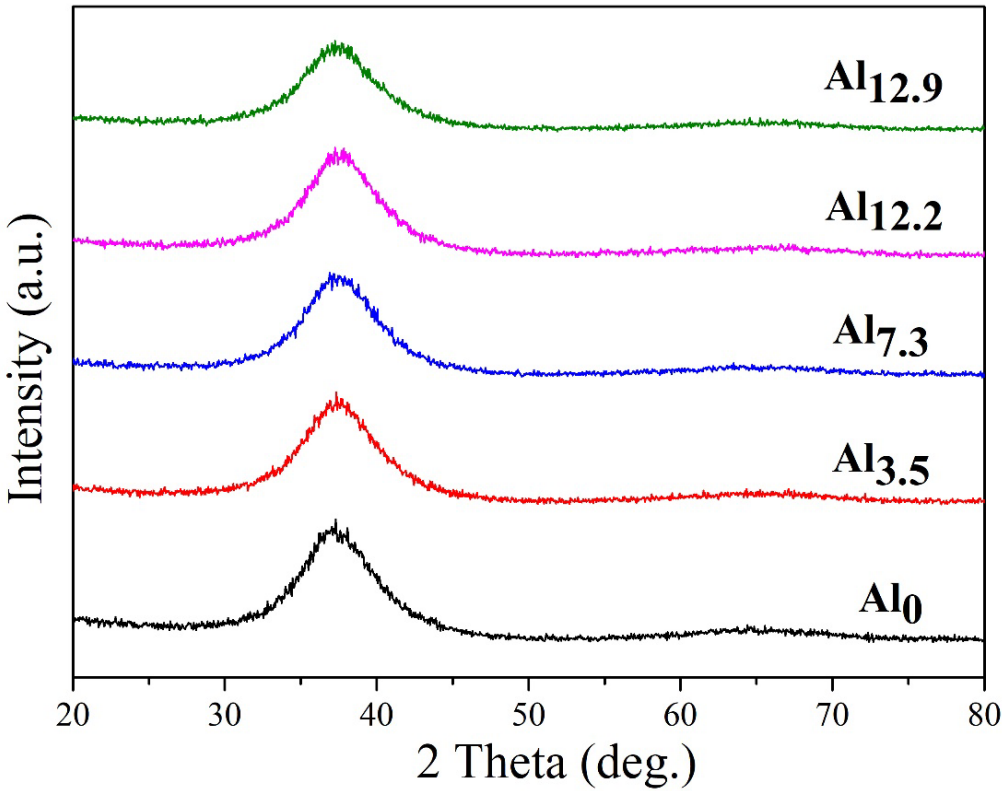

Fig. 4-1 XRD patterns of $(NbTiVZr)_{100-x}Al_x$ HEAFs with a scan rate of 4°/min.

Inoue [73] raised the following three empirical rules for improving glass formability for bulks alloy in 1995:

1. Consisting of three or more elements.
2. Having atomic size differences of 12% or above among the elements.
3. Possessing large negative mixing enthalpies among the elements.

The amorphous phase can accommodate or relax the size difference because it has lesser coordination number. Also, high entropy effect enhances complete mutual solubility of different elements and large lattice distortion effect enhances the tendency to form amorphous structure and also reduces the driving force for grain growth.

doi:10.6342/NTU202300667

4.1.3 SEM Observations

The cross-sectional SEM images of the $(NbTiVZr)_{100-x}Al_x$ HEAFs with various Al contents are illustrated in Fig. 4-2 to observe the morphology of the films and to measure the film thickness. As the power applied on Al target increased, the film thickness increased from 1.25 to 1.43 μm. The enlarged cross-sectional SEM image is illustrated in Fig. 4-3 and vein patterns are observed in the SEM image. The mechanism of the formation of the vein patterns and the schematic illustration of fracture mechanism in amorphous phase were shown in Fig. 4-4 [74, 75].

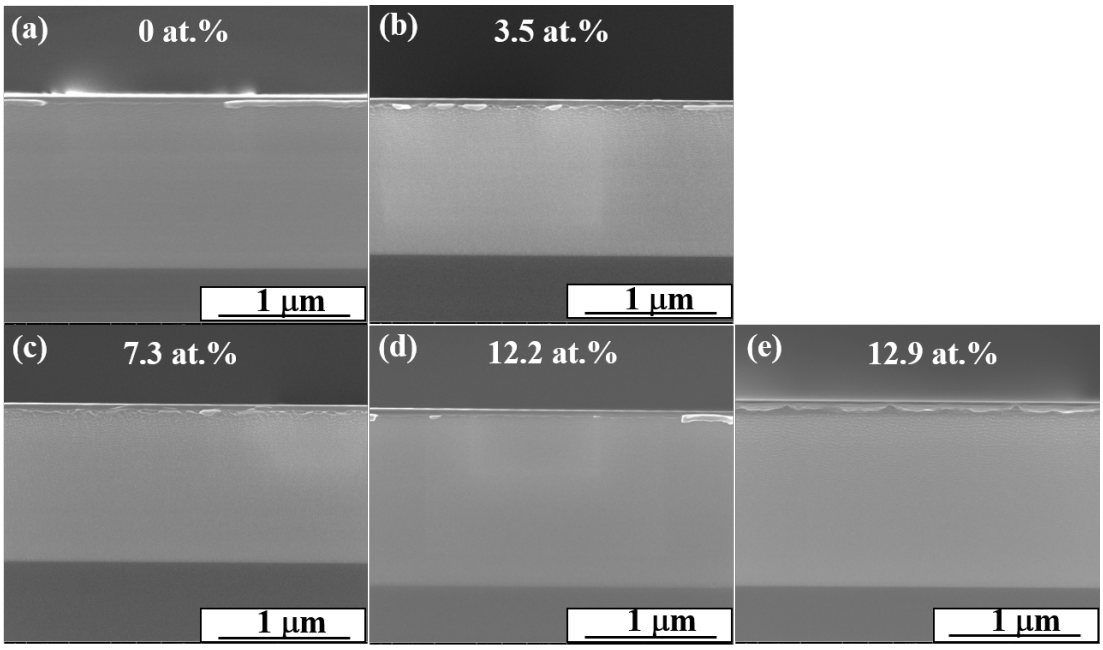

Fig. 4-2 Cross-sectional SEM images of the $(NbTiVZr)_{100-x}Al_x$ HEAFs with different Al contents: (a) Al_0, (b) $Al_{3.5}$, (c) $Al_{7.3}$, (d) $Al_{12.2}$, (e) $Al_{12.9}$ film.

doi:10.6342/NTU202300667

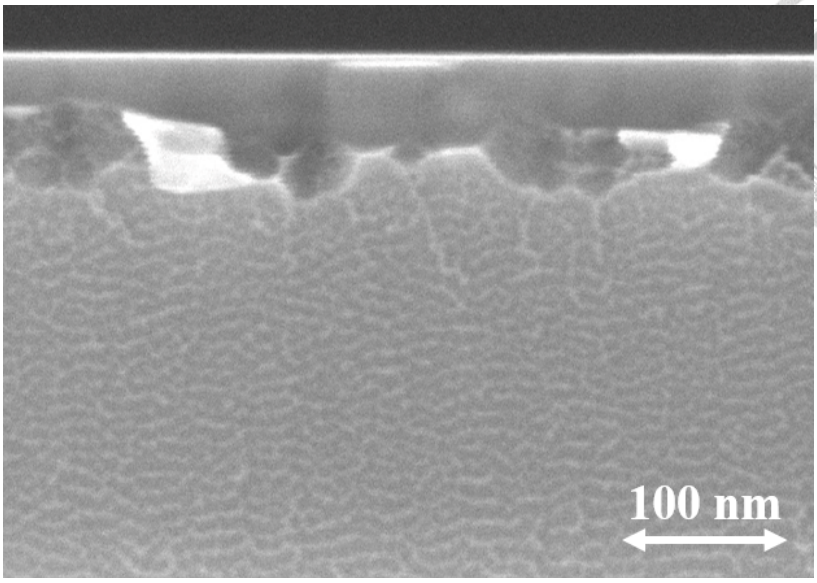

Fig. 4-3 The enlarged cross-sectional SEM images showed vein-patterns.

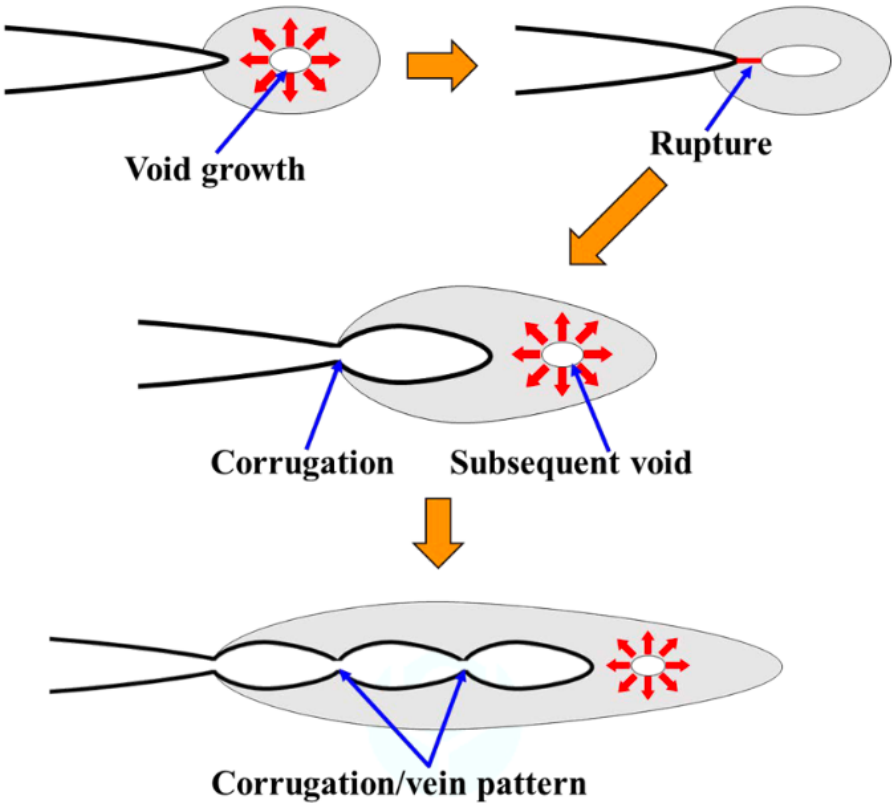

Fig. 4-4 Schematic illustration of the fracture mechanism in amorphous phase: voids in amorphous structures growth due to stress spreading, then rupture connects the void and crack tip. Repeatedly, stress spreads leading subsequent void growth. Rupture keeps connecting void and subsequent void, thereby ultimate occurring fracture. Therefore, vein pattern generated on this rupture surface.

doi:10.6342/NTU202300667

4.1.4 TEM Observations

The cross-sectional bright field (BF) TEM images, high resolution TEM (HRTEM) images and the corresponding fast Fourier transform (FFT) patterns for the Al_0 and $Al_{12.9}$ films in the $(NbTiVZr)_{100-x}Al_x$ HEAFs series are shown in Fig. 4-5. The amorphous halo rings without any diffraction spots were identified in both films, and the results confirmed the maintenance of amorphous structure. The cross-sectional TEM images were consistent with the XRD results presented in Fig. 4-1.

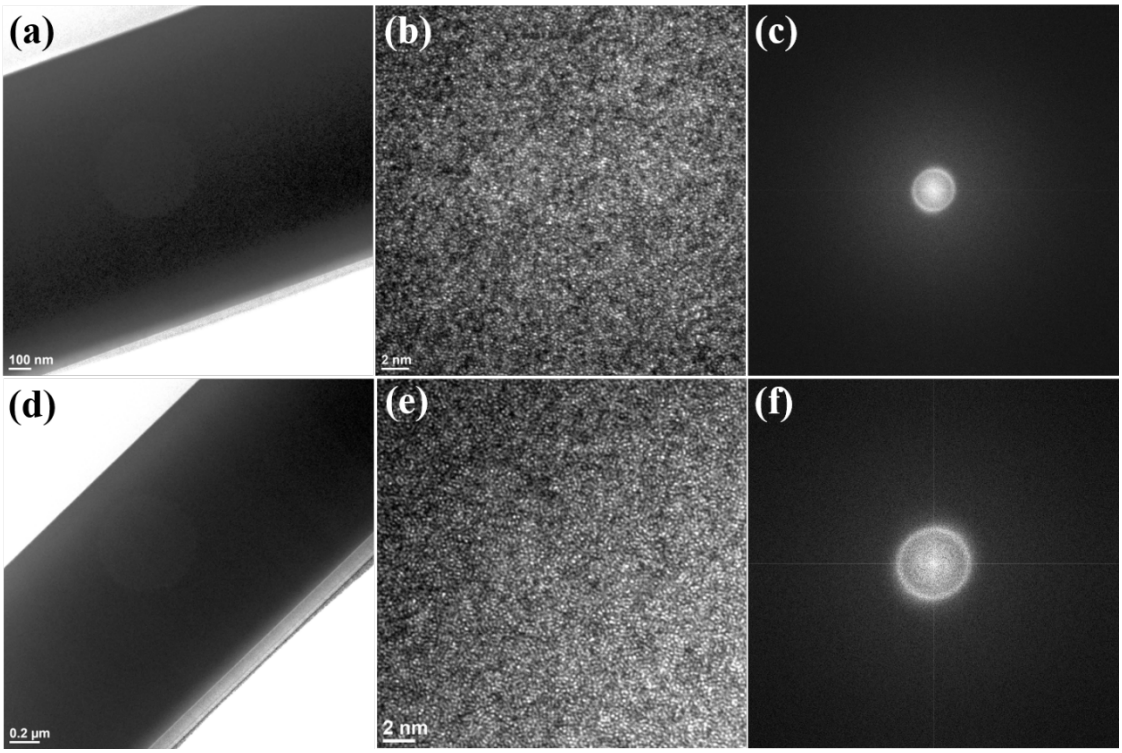

Fig. 4-5 The cross-sectional bright field TEM images of the $(NbTiVZr)_{100-x}Al_x$ HEAFs for (a) Al_0, and (d) $Al_{12.9}$ film. HRTEM image for (b) Al_0, and (e) $Al_{12.9}$ film and corresponding fast Fourier transform (FFT) images for (c) Al_0, and (f) $Al_{12.9}$ film.

4.1.5 Hardness and Reduced Modulus

Using nanoindentation, the measured hardness (H) and reduced modulus (E_r) of the $(NbTiVZr)_{100-x}Al_x$ HEAFs as functions of the Al content are shown in Fig. 4-6. Compared

doi:10.6342/NTU202300667

to the bulk counterparts, the HEAFs fabricated by rapid quenching method showed much smaller grain size because the fast cooling rate during the deposition inhibited the grain growth and led to the solid solution phase without precipitates. Therefore, the mechanical properties of $(NbTiVZr)_{100-x}Al_x$ HEAFs were much harder than as-cast bulk $(NbTiVZr)_{100-x}Al_x$ counterparts [34, 35]. With the Al addition, the hardness and reduced modulus of $(NbTiVZr)_{100-x}Al_x$ HEAFs increased slightly. In combination with the microstructures in the paragraphs above, the addition of Al has little affects due to the strong amorphization of the HEAFs.

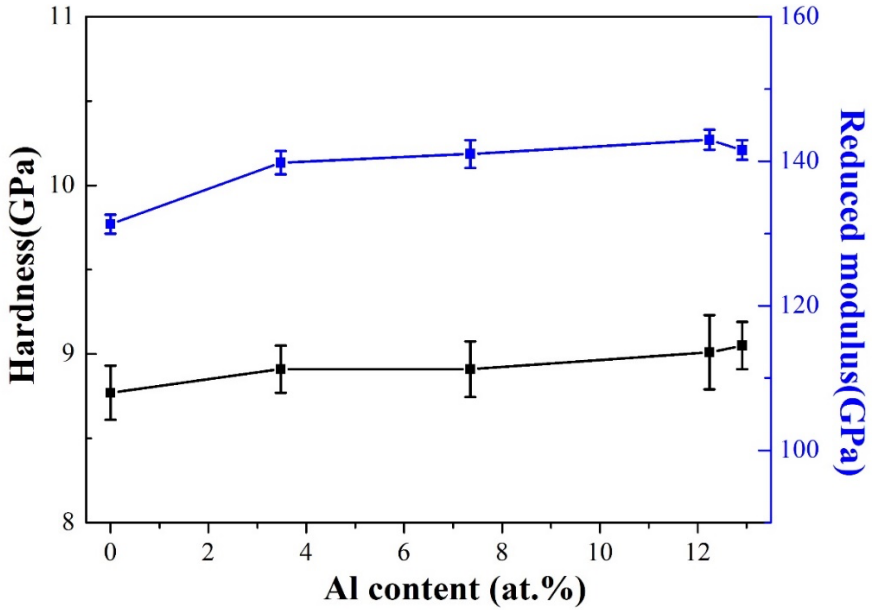

Fig. 4-6 The hardness and reduced modulus of the $(NbTiVZr)_{100-x}Al_x$ HEAFs films as functions of Al content.

4.2 $(NbTiVZrN)_{100-x}Al_x$ HEANFs

4.2.1 Chemical Compositions

The chemical compositions of the $(NbTiVZrN)_{100-x}Al_x$ HEANFs analyzed by EPMA

doi:10.6342/NTU202300667

are presented in Table 4-2. The content of Al increased from 0.7 to 4.0 at.% as the power applied on Al target increased from 50 W to 175 W. The concentrations of Nb, Ti, V, Zr were nearly equimolar and the slightly deviation could be attributed to the different sputtering yields of each element. For convenience, the $(NbTiVZrN)_{100-x}Al_x$ HEANFs were donated as Al_x film hereafter.

Table 4-2 The chemical compositions (at.%) of $(NbTiVZrN)_{100-x}Al_x$ HEANFs with different powers applied on Al target.

Power (W)	x	Chemical compositions (at.%)					
		Nb	Ti	V	Zr	N	Al
0	0	10.59± 0.04	14.96± 0.05	12.43± 0.11	12.03± 0.08	49.98± 0.21	0.00± 0.00
50	0.7	11.49± 0.11	13.94± 0.12	12.45± 0.12	11.02± 0.14	50.43± 0.39	0.70± 0.02
100	2.3	11.10± 0.14	13.99± 0.14	12.35± 0.05	11.08± 0.17	49.15± 0.28	2.31± 0.02
150	3.6	10.24± 0.16	13.87± 0.13	11.91± 0.11	11.02± 0.19	49.33± 0.47	3.61± 0.04
175	4.0	9.17± 0.04	12.40± 0.06	9.95± 0.13	10.05± 0.03	54.41± 0.12	4.00± 0.02

4.2.2 XRD Results

The XRD patterns of $(NbTiVZrN)_{100-x}Al_x$ HEANFs are shown in Fig. 4-7(a). Without Al addition, NbTiVZr nitride films exhibited FCC structure with an evident TiN(200) peak. However, as the Al content increased, the preferred orientation of the films gradually transferred from TiN(200) to (Nb, Zr)N(111) because of the high affinity between Ti and Al, and the depletion of Ti promoted the formation of (Nb, Zr)N, which had the (111) preferred orientation. Using a slower scan rate of 1°/min to observe the

doi:10.6342/NTU202300667

details of (200) peak, Fig. 4-7(b) shows the shift of (200) diffraction peaks to smaller diffraction angle and hence the increasing lattice parameter with the increasing Al content in the films [72]. The grain size (D) of the film was calculated using the Scherrer's formula, such that [76]

$$D = \frac{0.9\lambda}{B\cos\theta} \tag{6}$$

where λ is the wavelength of the incident Cu Kα X-ray, B is the full width at half maximum (FWHM) of the diffraction peak and θ is the diffraction angle (in radian). The grain size of the films increased with the increasing Al content as listed in Table 4-3. The increase of the grain size was due to the fact that the higher power applied on Al target enhanced the energetic ion bombardment which would promote the mobility of atoms and contribute to the increase of the grain size [65-67].

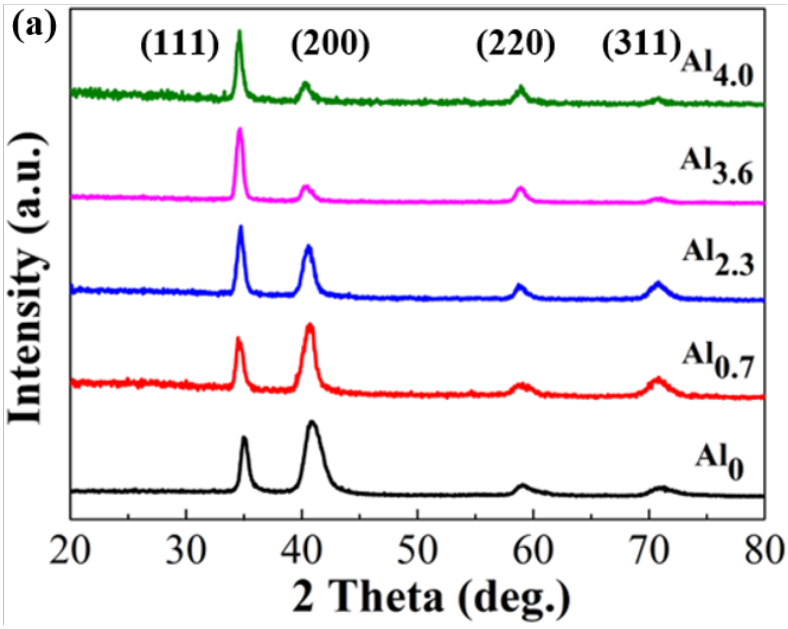

doi:10.6342/NTU202300667

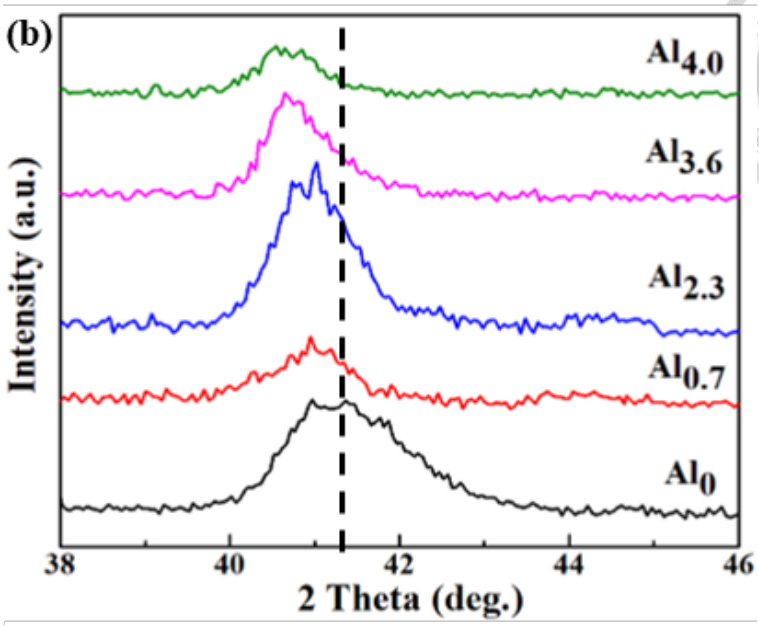

Fig. 4-7 XRD patterns of $(NbTiVZrN)_{100-x}Al_x$ HEAFs with a scan rate of (a) 4°/min and (b) 1°/min in the 2θ range from 38° to 46° to show the details of (200) peak.

Table 4-3 The full widths at half maximum (FWHM) and grain sizes calculated using Scherrer's formula from XRD spectra.

Films	Al_0	$Al_{0.7}$	$Al_{2.3}$	$Al_{3.6}$	$Al_{4.0}$
FWHM	0.029	0.020	0.019	0.017	0.015
Grain size (nm)	5.17	7.25	7.78	8.57	9.87

The mixing enthalpies for different binary components in NbTiVZrAlN system are listed in Table 4-4 [33]. Owing to the large negative values of mixing enthalpy between the nitrogen and other constituent elements, the $(NbTiVZrN)_{100-x}Al_x$ HEAFs were dominated by the nitride compounds, such as TiN, NbN and ZrN. Nevertheless, the high affinity between Ti and Al still effectively influenced the constitution of the films by robbing Ti away from TiN and forming HCP-Ti_3Al. Unlike other nitride compounds, the presence of Ti_3Al in $(NbTiVZrN)_{100-x}Al_x$ films was not found in XRD results shown in

doi:10.6342/NTU202300667

Fig. 4-7(a). However, the presence of HCP-Ti_3Al would be proven in HRTEM results. Consequently, the depletion of Ti would promote the formation of (Nb, Zr)N in the films.

Table 4-4 Mixing enthalpies ΔH (kJ/mol) for different binary components in NbTiVZrAlN system.

Element	Al	Nb	Ti	V	Zr	N
Al	–	-18	-30	16	-44	-92
Nb	–	–	2	-1	4	-174
Ti	–	–	–	-2	0	-190
V	–	–	–	–	-4	-143
Zr	–	–	–	–	–	-233
N	–	–	–	–	–	–

4.2.3 SEM Observations

The cross-sectional SEM images of the $(NbTiVZrN)_{100-x}Al_x$ HEAFs with various Al contents are illustrated in Fig. 4-8 to observe the morphology of the films and to measure the film thickness. All the films showed fiber-like columnar structures, and the columnar growth direction was perpendicular to the substrate surface during the sputtering process. As the power applied on Al target increased, the film thickness increased from 1.19 to 1.31 μm presented in Fig. 4.8(f). Compared to the $(NbTiVZr)_{100-x}Al_x$ HEAFs without nitride, the thickness of nitride films was much smaller due to the nitrogen absorption on or even nitridation of the target surface, leading to a decrease in sputtering efficiency. This phenomenon is a typical result of the well-known target poisoning [7, 69]. All the films showed good bonding with Si substrates and exhibited compact structure with a few inclusions and voids. Due to the fact that the Al_0 film exhibited the bilayered structure with featureless bottom layer and columnar-structured

doi:10.6342/NTU202300667

top layer shown in Fig. 4-8(a), the structures of Al_0 film were further identified by HRTEM in the following.

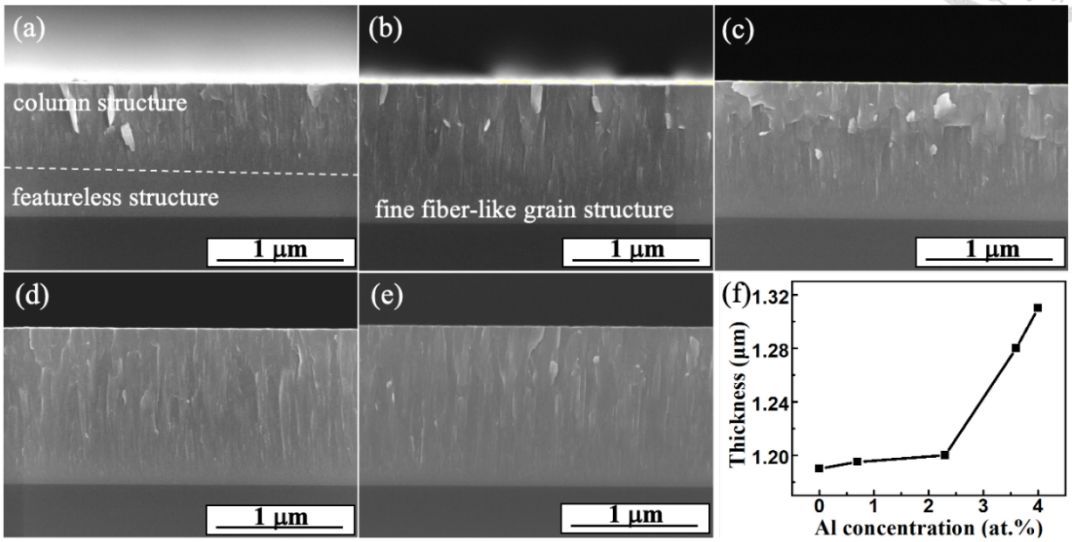

Fig. 4-8 Cross-sectional SEM images of the $(NbTiVZrN)_{100-x}Al_x$ HEANFs with different Al contents: (a) Al_0, (b) $Al_{0.7}$, (c) $Al_{2.3}$, (d) $Al_{3.6}$, (e) $Al_{4.0}$. (f) The film thickness as a function of Al concentration.

4.2.4 TEM Observations

The cross-sectional bright field (BF) TEM image of Al_0 film is shown in Fig. 4-9(a), and it revealed featureless bottom layer and columnar-structured top layer in agreement with the cross-sectional SEM image shown in Fig. 4-9(a). The high-resolution transmission electron microscopy (HRTEM) image of the white circled area within columnar top layer in Fig. 4-9(a) is shown in Fig. 4-9(b), and lattice fringes could be observed. The fast Fourier transform (FFT) image of the framed area in Fig. 4-9(b) is shown in Fig. 4-9(c), showing the fully-crystallized FCC structure. The HRTEM image of the red circled area within featureless bottom layer in Fig. 4-9(a) is shown in Fig. 4-9(d), revealing the coexistence of nanocrystalline and amorphous phase. To further

doi:10.6342/NTU202300667

investigate the detailed microstructure, the corresponding FFT patterns of the white and the yellow squares marked in Fig. 4-9(d) are illustrated in Fig. 4-9(e) and (f), respectively. The results of the corresponding FFT patterns confirmed that the bottom layer of the film consisted of nanocrystalline grains embedded in amorphous structure.

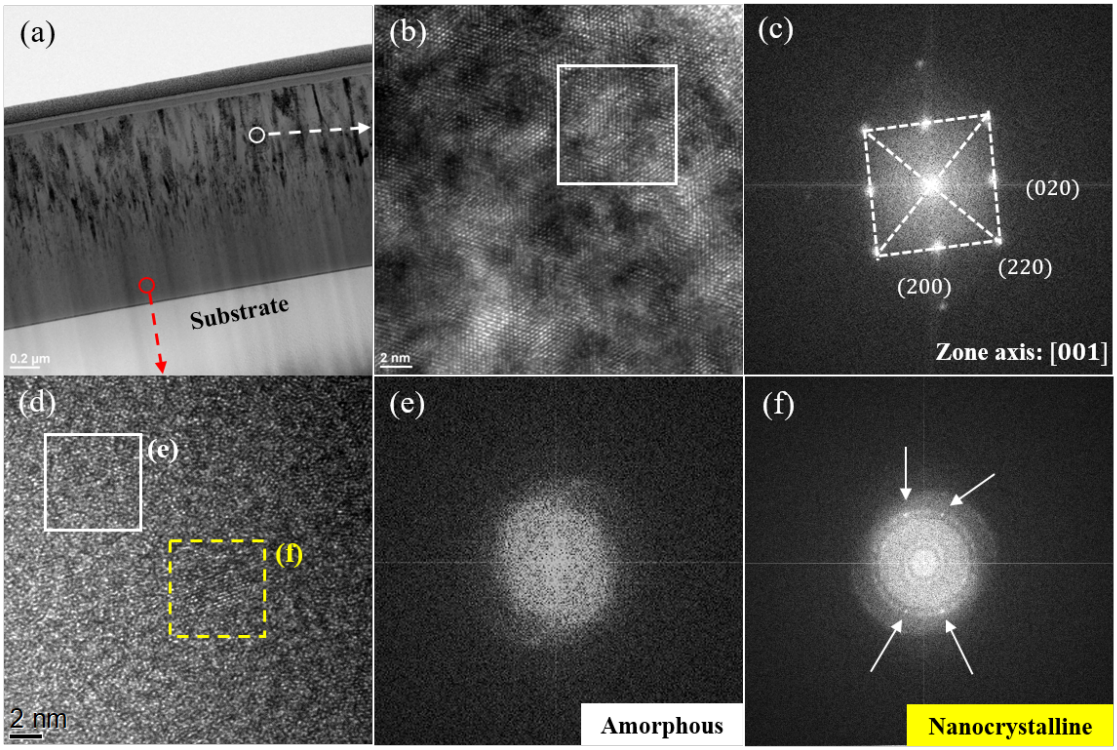

Fig. 4-9 (a) The cross-sectional BF TEM image of Al0 film, showing the bilayered structure, (b) the HRTEM image of the white circled area in (a) showing the lattice fringes, (c) the FFT patterns taken from the framed area in (b), revealing the FCC structure, (d) the HRTEM image in the red circle area in (a) and the FFT patterns taken from (e) the white framed area in (d) revealing the amorphous structure and (f) the yellow framed area in (d) revealing nanocrystalline structure.

To examine the detailed morphologies of the films and to confirm the XRD results, TEM was employed. The cross-sectional BF TEM images and the corresponding selected area electron diffraction (SAED) patterns of $(NbTiVZrN)_{100-x}Al_x$ HEANFs are displayed in Fig. 4-10. For the BF images of the films, the nano-sized columnar structure normal to the substrate was identified and the structure was confirmed to be FCC phase based on

doi:10.6342/NTU202300667

the corresponding SAED patterns. The lattice constant of the $(NbTiVZrN)_{100-x}Al_x$ HEANFs could be calculated using the following equation [77]:

$$\frac{1}{d^2_{hkl}} = \frac{h^2+k^2+l^2}{a^2} \quad (7)$$

where d_{hkl} is the lattice spacing of the (*hkl*) plane, *a* is the lattice parameter of the materials. The lattice constants of the TiN, ZrN and NbN compounds have been measured elsewhere [78-80] and are listed in Table 4-5. The lattice parameter of the Al_0 film calculated from SAED pattern in Fig. 4-10(b) was 0.423 nm, which was similar to the lattice constant of TiN (0.424 nm) shown in Table 4-5. However, as the Al content increased to 4.0 at.%, the calculated lattice parameter from Fig. 4-10(j) increased to the maximum value of 0.451 nm shown in Table 4-6. The difference in the lattice parameter between the films with different Al concentrations indicated that the dominant compounds were not TiN but (Nb, Zr)N instead for $Al_{4.0}$ film. The results were consistent with XRD results shown in Fig. 4-7(a).

doi:10.6342/NTU202300667

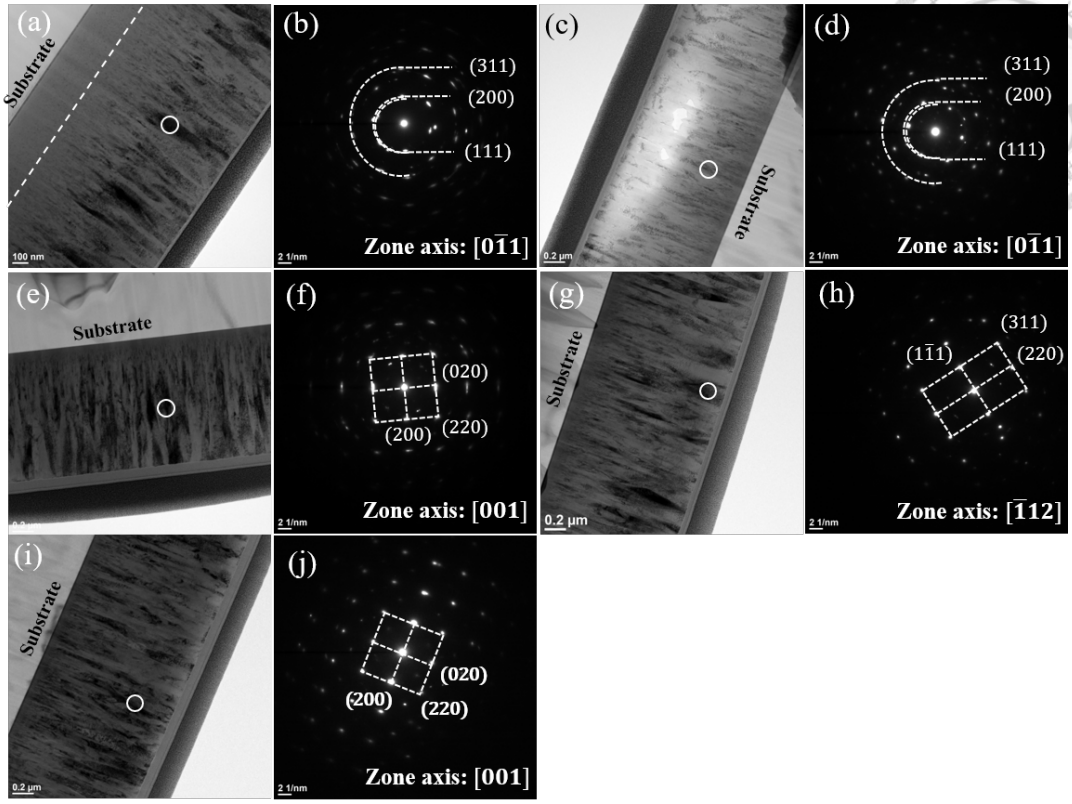

Fig. 4-10 TEM images of the films and the corresponding SAED patterns. (a, b) Al_0, (c, d) $Al_{0.7}$, (e, f) $Al_{2.3}$, (g, h) $Al_{3.6}$, (i, j) $Al_{4.0}$ film.

Table 4-5 Lattice constants measured in previous researches [78-80].

Nitride compounds	Lattice constant (nm)
TiN	0.424 [78]
ZrN	0.457 [79]
NbN	0.439 [80]

Table 4-6 Lattice constants calculated from SAED patterns shown in Fig. 4-10(b), 4(d), 4(f), 4(h), 4(j).

Films	Lattice constant (nm)
Al_0	0.423
$Al_{0.7}$	0.430
$Al_{2.3}$	0.432
$Al_{3.6}$	0.437
$Al_{4.0}$	0.451

The HRTEM image of the $Al_{0.7}$ film is shown in Fig. 4-11(a) and the FFT pattern of the framed area in Fig. 4-11(a) is presented in Fig. 4-11(b) in order to further identify the existence of HCP-Ti_3Al in Al-doped NbTiVZr nitride films. The HCP phase along [0001]

doi:10.6342/NTU202300667

direction was observed in $Al_{0.7}$ film through calculating the angle and the distance between the incident spot and the diffraction spots. The presence of HCP phase provided the evidence of the formation of HCP-Ti_3Al compound in Al-doped NbTiVZr nitride films.

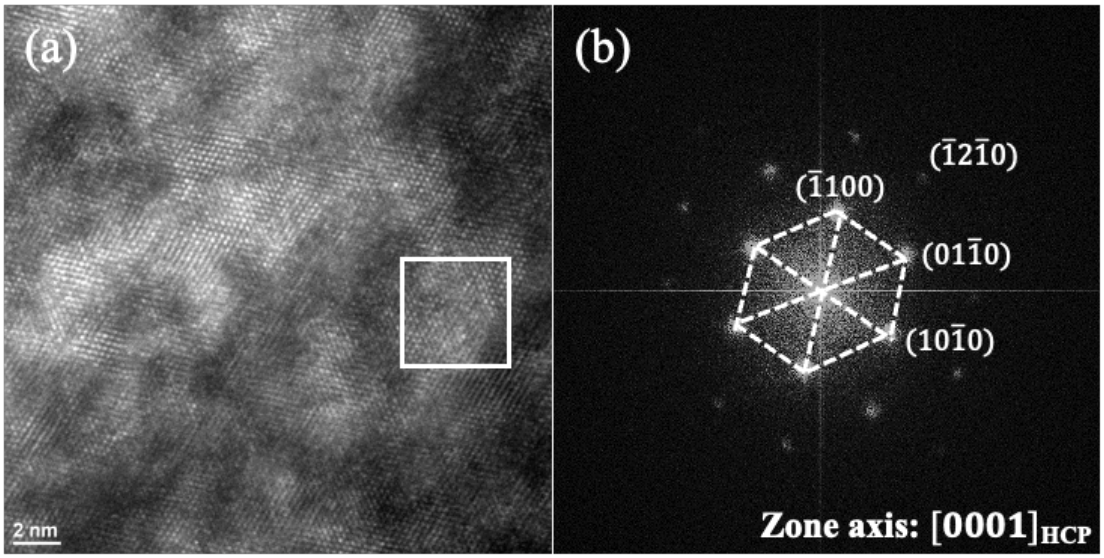

Fig. 4-11 (a) The HRTEM image of Al0.7 film and (b) the FFT pattern of white framed area marked in (a), indicating HCP along [0001] direction.

The TEM-EDS mapping was conducted to analyze the elemental distribution of $Al_{3.6}$ film. With the bright field TEM image shown in Fig. 4-12(a), the element distributions of the $Al_{3.6}$ film are shown in Fig. 4-12(b). The six constituent elements of the film were uniformly distributed without notable segregation or precipitates over a wide region, indicating that $Al_{3.6}$ film was homogeneous. The homogeneity of the elemental distributions could also be found in other $(NbTiVZrN)_{100-x}Al_x$ HEANFs in the present work.

doi:10.6342/NTU202300667

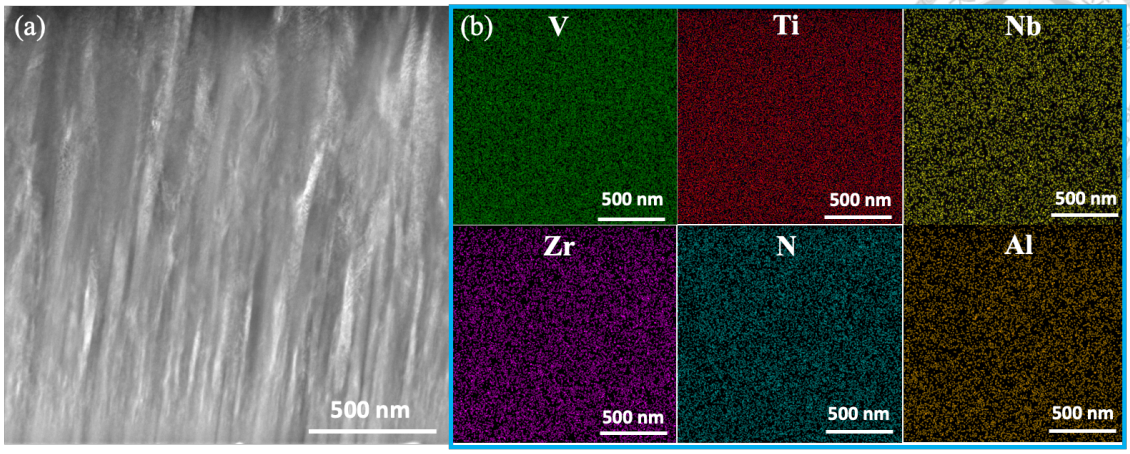

Fig. 4-12 (a) The bright field TEM image and (b) EDS mapping of the $Al_{3.6}$ film.

4.2.5 XPS results

To further confirm the chemical bonding status of the $(NbTiVZrN)_{100-x}Al_x$ HEANFs, XPS measurements were conducted for the Al_0 and $Al_{3.6}$ films. Compared to Al_0 film (Fig. 4-13(a)), $Al_{3.6}$ film (Fig. 4-13(b)) showed the shift of the binding energy of the N 1s spectrum from 397.3 to 396.9 eV. The N 1s spectrum could be deconvoluted into four sub-spectra and all the contributions included TiN, NbN, ZrN, AlN and VN compounds ascribed to 397.4, 397.1, 396.7, 397.8 and 397.7 eV, respectively [81-86]. The results indicated that a considerable TiN species existed in Al_0 film while a little TiN presented in $Al_{3.6}$ film. On the other hand, as the Al content increased to 3.6 at.%, the amount of TiN decreased significantly and a larger portion of NbN and ZrN was found instead. The results agreed well with the XRD results shown in Fig. 4-7.

doi:10.6342/NTU202300667

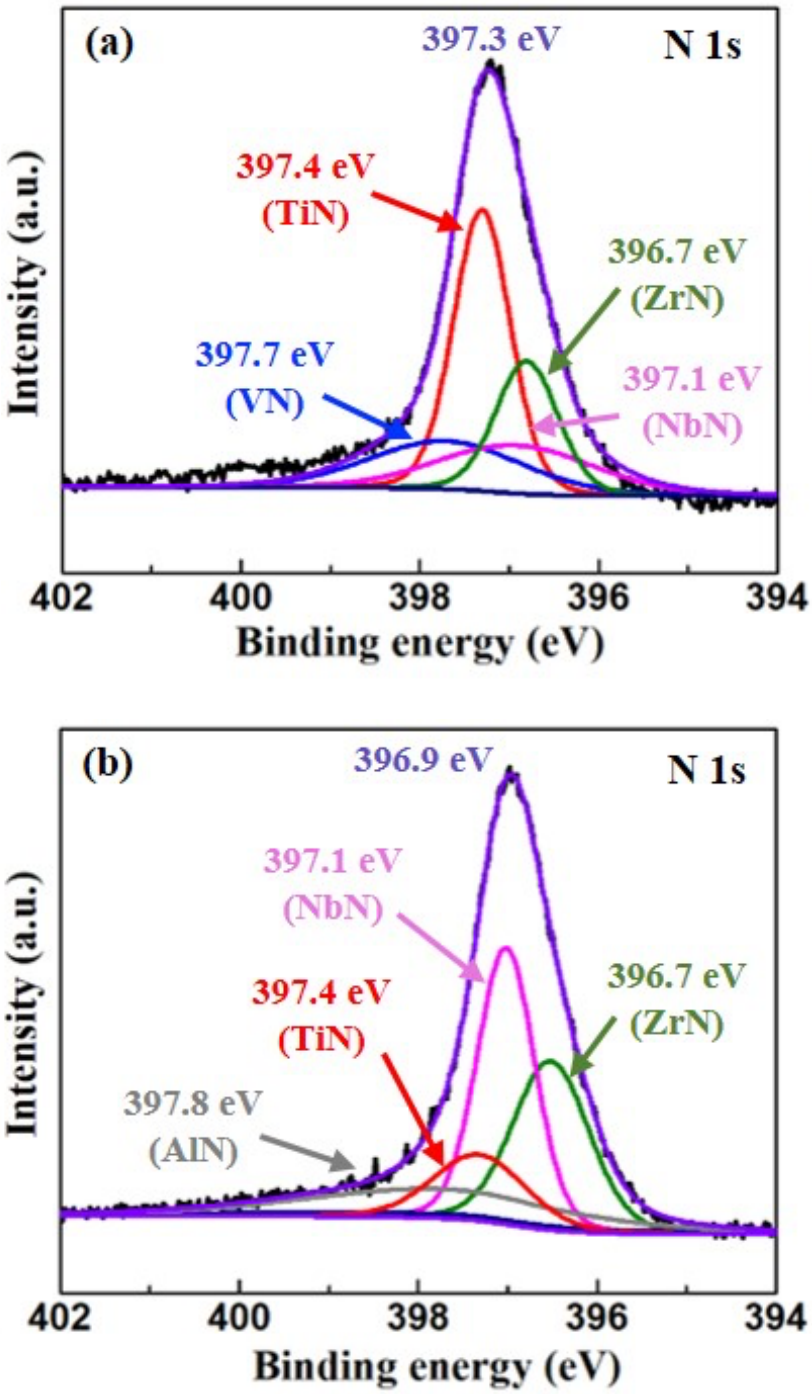

Fig. 4-13 XPS deconvolution results of N 1s for the (a) Al_0 and (b) $Al_{3.6}$ film.

4.2.6 Hardness and Reduced Modulus

Using nanoindentation, the measured hardness (H) and reduced modulus (E_r) of the $(NbTiVZrN)_{100-x}Al_x$ HEANFs as functions of the Al content are shown in Fig. 4-14. The Al_0 film with the bilayered structure showed H and E_r of about 24.5 and 229.6 GPa,

doi:10.6342/NTU202300667

respectively, which were similar to the reported results of HEANFs elsewhere [15, 23]. The presence of amorphous phase would introduce free volumes to result in a lower density compared with the crystalline counterparts [87]. However, as the Al content increased, the value of H and E_r increased with the fully-crystallized structure and reached the maximum of 28.1 and 253.0 GPa, respectively, for $Al_{3.6}$ film, and then decreased with the further increase in Al content. The initial improvement in H and E_r could be attributed to the following reasons:

(i) Solid solution strengthening: The incorporation of extra solute elements in solid solution to strengthen the films is a common technique performed by the previous researches. The solid solution strengthening is caused by the lattice distortion, and the severe lattice expansion makes the lattice parameter larger.

(ii) Inverse Hall-Petch: Commonly, the difficulty for dislocations to propagate through the materials mainly determines the mechanical properties of the materials, and the refinement of grain size can offer more grain boundaries to hinder the dislocation motion. The mechanical properties are improved as the dislocation slips more difficultly. The phenomenon is called Hall-Petch relationship [88]. However, when the grain size is less than the critical value of ~10 nm, the mechanism of plastic deformation becomes dominated by grain boundary sliding and grain boundary softening, causing the inverse Hall-Petch

doi:10.6342/NTU202300667

effect [89-91]. Consequently, due to the fact that all the calculated grain size listed in Table 2 were less than ~10 nm, the initial enhancement of H and E_r could be explained by the inverse Hall-Petch effect in this research.

(iii) Replacement of dominant nitride compounds: The hardness of TiN, NbN and ZrN were ~25, ~30 and ~26 GPa, respectively, presented in the previous studies [92-95]. The enhancement of the hardness from 24.5 GPa (Al_0) to 28.1 GPa ($Al_{3.6}$) could also be attributed to the replacement of the dominant nitride compounds.

With the further addition of Al content, the H and E_r decreased slightly to the value of 26.7 and 247.3 GPa, respectively, for $Al_{4.0}$ film. Presented results indicated that there is an optimum value of the Al dopant for 3.6 at.%. When more Al atoms were added into the HEANFs, which exceeded the solubility limit of Al, the $Al_{4.0}$ film with more ductile HCP-Ti_3Al phase would consequently exhibit lower H and E_r.

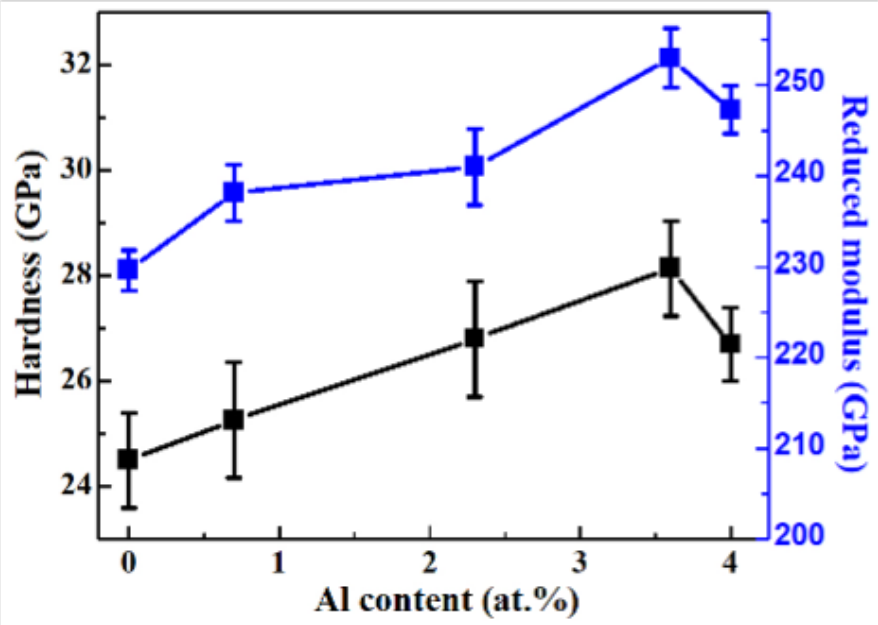

doi:10.6342/NTU202300667

Fig. 4-14 The hardness and reduced modulus of the $(NbTiVZrN)_{100-x}Al_x$ HEANFs films as functions of Al content.

4.2.7 Fracture toughness

The fracture toughness represents its ability to absorb the energy during the deformation until the failure of the material. The fracture toughness of the $(NbTiVZrN)_{100-x}Al_x$ HEANFs shown in Fig. 4-15 increased from the value of 1.30 $MPa \times m^{0.5}$ for Al_0 film to reach the maximum value of 2.08 $MPa \times m^{0.5}$ for $Al_{3.6}$ film. Compared to nitride compounds, Ti_3Al intermetallic compound was proved to be ductile phase presented in the previous researches [96, 97]. The improvement of fracture toughness could result from the incorporation of the HCP phase (Ti_3Al compound) which overcame the brittleness of nitride films through ductile phase toughening [98]. The measured H, E_r, K_C and the values of H^3/E^2 ratios are listed in Table 4-7. According to the previous works, the H/E and H^3/E^2 ratios could be considered as an index of the resistance against elastic strain and plastic deformation should be related to the value of fracture toughness [99]. The dependence of H^3/E^2 ratios on the Al content was highly correlated to the fracture toughness of the films in this research. The indents using the nanoindentation with the slow scan of 0.5 Hz is shown in Fig. 4-16.

doi:10.6342/NTU202300667

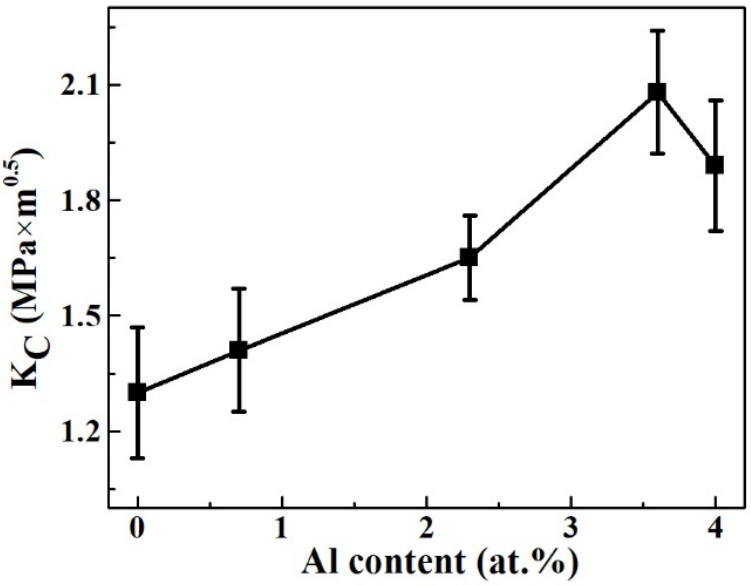

Fig. 4-15. The fracture toughness of the $(NbTiVZrN)_{100-x}Al_x$ HEANFs as a function of Al content.

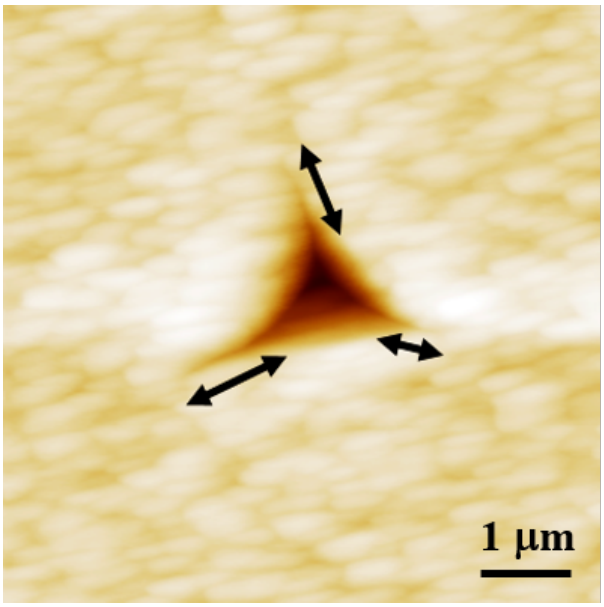

Fig. 4-16 The images of indent using the nanoindentation with the slow scan of 0.5 Hz.

Table 4-7. The measured hardness, reduced modulus, K_C and H^3/E^2 from the nanoindentation test of the $(NbTiVZrN)_{100-x}Al_x$ HEANFs.

Films	**Hardness (GPa)**	E_r **(GPa)**	H^3/E^2 **(GPa)**	K_C **(MPa×m$^{0.5}$)**
Al_0	24.5±0.9	229.6±2.3	0.19	1.30±0.17
$Al_{0.7}$	25.3±0.1	238.1±3.1	0.20	1.41±0.16
$Al_{2.3}$	26.8±1.1	241.0±4.4	0.22	1.65±0.11
$Al_{3.6}$	28.1±0.9	253.0±2.3	0.23	2.08±0.16

doi:10.6342/NTU202300667

$Al_{4.0}$	26.7±0.7	247.3±2.6	0.21	1.89±0.17

The comparison of the hardness and fracture toughness between $(NbTiVZrN)_{100-x}Al_x$ HEANFs in the present work and other nitride films in previous researches [100-102] is shown in Fig. 4-17. It could be noted that most of the films exhibited the K_{IC} value below 1.5 MPa×$m^{0.5}$, while both K_C and H of $(NbTiVZrN)_{100-x}Al_x$ HEANFs in the present work were higher than most of others. In addition, the $Al_{3.6}$ film possessed the optimum combination of K_C (= 2.08 MPa×$m^{0.5}$) and H (= 28.1 GPa).

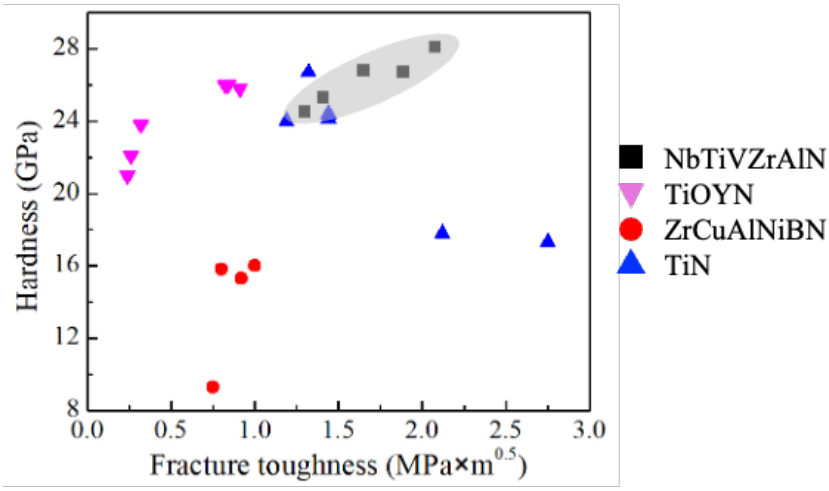

Fig. 4-17. Comparison of hardness and fracture toughness between HEANFs in this work and some previous researches [100-102] on other nitride films.

4.2.8 Nanoscratch results

Nano-scratch tests were conducted to determine the load bearing capacity of the film subjected to both normal and tangential forces, and the coefficient of friction (COF) of the film could be obtained by dividing the lateral tangential force by the normal force [103]. The average coefficients of friction of $(NbTiVZrN)_{100-x}Al_x$ HEANFs with different

doi:10.6342/NTU202300667

Al contents are shown in Fig. 4-18. The COF slightly decreased from 0.082 to 0.065 with the increasing Al content, and the minimum value (0.065) was obtained in $Al_{4.0}$ film. Basically, the mechanical properties of the films determine its tribological properties. The higher mechanical properties are more resistant to plastic deformation under certain applied loads, hence the improvement of the coefficient of friction possessed a similar trend with the H^3/E^2 value as well [63]. In addition, the steady tendency of coefficient of friction shown in Fig. 4-18 could be reasonably attributed to the uniform and smooth film's surface. The normal displacement, normal force and lateral force as the functions of scratch time was illustrated in Fig. 4-19, and the maximum value of the normal displacement was about ~50 nm as the normal force increased to 5000 μN.

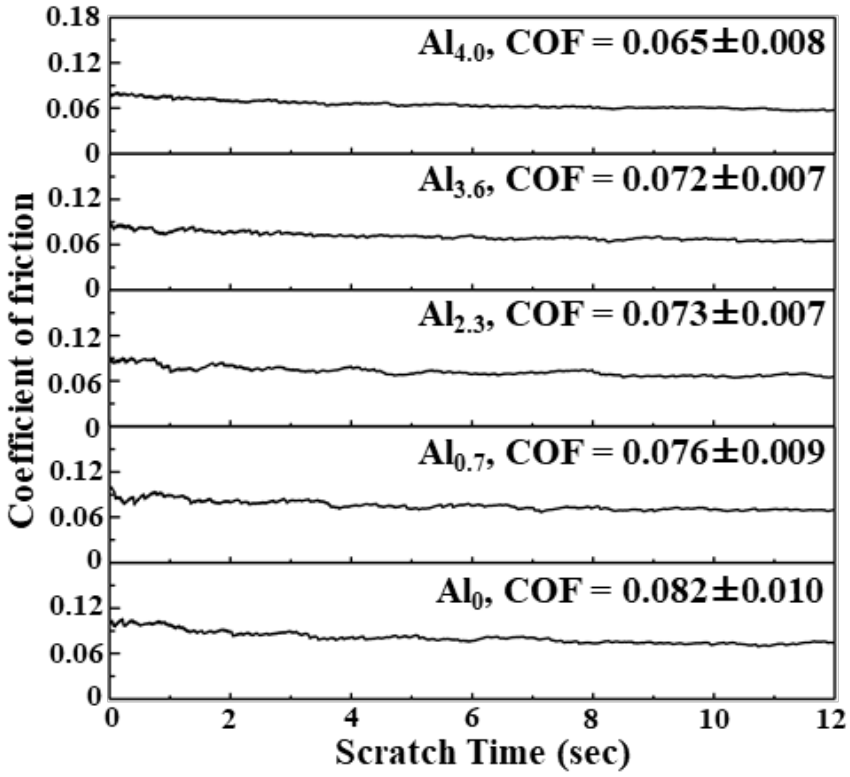

Fig. 4-18. The average coefficient of friction for the $(NbTiVZrN)_{100-x}Al_x$ HEANFs as a function of scratch

doi:10.6342/NTU202300667

time.

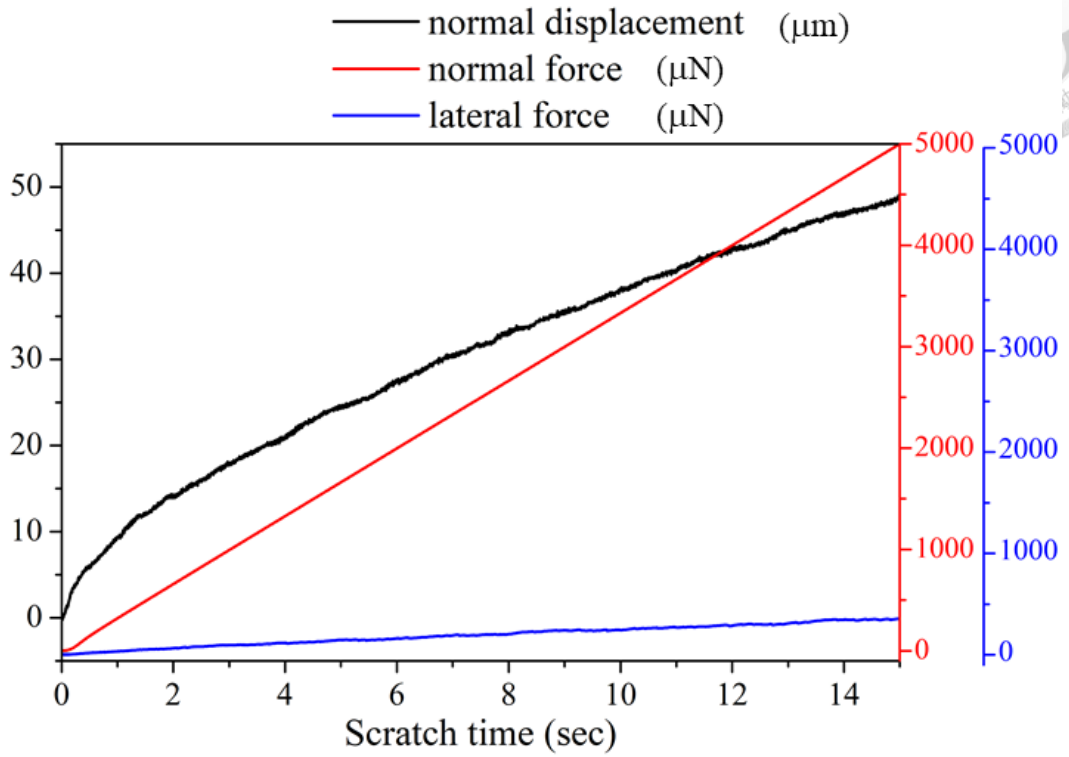

Fig. 4-19 The normal displacement, normal force and lateral force as the functions of scratch time.

Chapter 5 Conclusions

5.1 $(NbTiVZr)_{100-x}Al_x$ HEAFs

From the XRD spectra, it can be seen that all the $(NbTiVZr)_{100-x}Al_x$ HEAFs with different Al content presented a single low-intensity wide peak. The results indicated all the films exhibited amorphous phase. For the cross-sectional SEM images, all the films showed structures with vein patterns. As the power applied on Al target increased, the film thickness increased from 1.25 to 1.43 μm. The amorphous halo rings without any diffraction spots shown in TEM images were identified in Al_0 and $Al_{12.9}$ films, and the results confirmed the maintenance of amorphous structure.

doi:10.6342/NTU202300667

5.2 $(NbTiVZrN)_{100-x}Al_x$ HEANFs

In summary, the $(NbTiVZrN)_{100-x}Al_x$ (x=0, 0.7, 2.3, 3.6, 4.0) HEANFs were deposited by magnetron co-sputtering of NbTiVZr alloy target and Al target with a constant N_2/Ar flow ratio, and the effects of Al addition on their microstructures associated with the corresponding mechanical properties were systematically investigated. The following results could be drawn:

1. Without Al addition, the nitride films presented FCC structure with the evident TiN(200) peak. However, the preferred orientation of the film gradually transferred from (200) to (111) with the increasing Al content because of the formation of HCP-Ti_3Al, and the depletion of Ti promoted the formation of (Nb, Zr)N, which had the (111) preferred orientation.
2. XPS was conducted to investigate the chemical bonding status of the nitride films, especially for the Al_0 and $Al_{3.6}$ films. The results agreed well with the XRD results.
3. All the films presented fine-columnar structure and the columnar growth direction was perpendicular to the substrate surface. The Al_0 film exhibited the bilayered structure with columnar-structured top layer and featureless bottom layer consisted of nanocrystalline grains embedded in amorphous matrix, while other films in the $(NbTiVZrN)_{100-x}Al_x$ HEANFs with Al additions presented highly crystallized grains.
4. Nanoindentation tests showed that as the Al concentration increased, the hardness

doi:10.6342/NTU202300667

and reduced modulus of the films increased and reached the maximum at 28.1 and 253 GPa, respectively, for $Al_{3.6}$ film. The improvement could be attributed to solid solution strengthening, inverse Hall-Petch and the replacement of dominant compounds.

5. The enhancement of fracture toughness could be attributed to the ductile phase toughening. The fracture toughness of the films increased with increasing Al content and reached the maximum value of 2.08 MPa×$m^{0.5}$ at $Al_{3.6}$ film. With the Al doping, the fracture toughness of $(NbTiVZrN)_{100-x}Al_x$ HEANFs in the present work was higher than most of the other nitride films in previous researches.

6. As the Al content increased, the COF value deceased from 0.082 to 0.065. It can be concluded that the nano-tribological performance of the Al-doped films is better than the Al-undoped film in the $(NbTiVZrN)_{100-x}Al_x$ HEAFs series.

References

[1] J.-W. Yeh, S.-K. Chen, S.-J. Lin, J.-Y. Gan, T.-S. Chin, T.-T. Shun, C.-H. Tsau, S.-Y. Chang, Nanostructured High-Entropy Alloys with Multiple Principal Elements:Novel AlloyDesign Concepts and Outcomes, *Adv. Eng. Mater.* **6** (2004) 299-303.

[2] M.-H. Tsai, J.-W. Yeh, High-Entropy Alloys: A Critical Review, *Mater. Res. Lett.* **2(3)** (2014) 107-123.

[3] J.-W. Yeh, Recent progress in high-entropy alloys, *Ann. Chim. (Cachan, Fr.)* **31(6)** (2006) 633-648.

[4] Y.S. Kim, H.J. Park, S.C. Mun, E. Jumaev, S.H. Hong, G. Song, J.T. Kim, Y.K. Park, K.S. Kim, S.I. Jeong, Y.H. Kwon, K.B. Kim, Investigation of structure and mechanical properties of TiZrHfNiCuCo high entropy alloy thin films synthesized

doi:10.6342/NTU202300667

by magnetron sputtering, *J. Alloys Compd.* **797** (2019) 834-841.

[5] H. Kim, S. Nam, A. Roh, M. Son, M.-H. Ham, J.-H. Kim, H. Choi, Mechanical and electrical properties of NbMoTaW refractory high-entropy alloy thin films, *Int. J. Refract. Met. Hard Mater.* **80** (2019) 286-291.

[6] X. Feng, J. Zhang, Z. Xia, W. Fu, K. Wu, G. Liu, J. Sun, Stable nanocrystalline NbMoTaW high entropy alloy thin films with excellent mechanical and electrical properties, *Mater. Lett* **210** (2018) 84-87.

[7] B. Ren, S.Q. Yan, R.F. Zhao, Z.X. Liu, Structure and properties of (AlCrMoNiTi)N_x and (AlCrMoZrTi)N_x films by reactive RF sputtering, *Surf. Coat. Technol.* **235** (2013) 764-772.

[8] X. Feng, G. Tang, M. Sun, X. Ma, L. Wang, K. Yukimura, Structure and properties of multi-targets magnetron sputtered ZrNbTaTiW multi-elements alloy thin films, *Surf. Coat. Technol.* **228** (2013) 424-427.

[9] P. Hruška, F. Lukáč, S. Cichoň, M. Vondráček, J. Čížek, L. Fekete, J. Lančok, J. Veselý, P. Minárik, M. Cieslar, O. Melikhova, T. Kmječ, M.O. Liedke, M. Butterling, A. Wagner, Oxidation of amorphous HfNbTaTiZr high entropy alloy thin films prepared by DC magnetron sputtering, *J. Alloys Compd.* **869** (2021) 157978.

[10] C.-Y. Cheng, J.-W. Yeh, High-entropy BNbTaTiZr thin film with excellent thermal stability of amorphous structure and its electrical properties, *Mater. Lett* **185** (2016) 456-459.

[11] W.-J. Sheng, X. Yang, J. Zhu, C. Wang, Y. Zhang, Amorphous phase stability of NbTiAlSiN_x high-entropy films, *Rare Met.* **37(8)** (2017) 682-689.

[12] Z. Wang, C. Wang, Y.-L. Zhao, T.-H. Huang, C.-L. Li, J.-J. Kai, C.-T. Liu, C.-H. Hsueh, Growth, microstructure and mechanical properties of CoCrFeMnNi high entropy alloy films, *Vacuum* **179** (2020) 109553.

[13] Y. Xu, G. Li, Y. Xia, Synthesis and characterization of super-hard AlCrTiVZr high-entropy alloy nitride films deposited by HiPIMS, *Appl. Surf. Sci.* **523** (2020) 146529.

[14] J.-W.Y. Ping-Kang Huang, Effects of nitrogen content on structure and mechanical properties of multi-element (AlCrNbSiTiV)N coating, *Surface & Coatings Technology* **203** (2009) 1891–1896.

[15] D.-C. Tsai, Z.-C. Chang, B.-H. Kuo, M.-H. Shiao, S.-Y. Chang, F.-S. Shieu, Structural morphology and characterization of (AlCrMoTaTi)N coating deposited via magnetron sputtering, *Appl. Surf. Sci.* **282** (2013) 789-797.

[16] H.-T. Hsueh, W.-J. Shen, M.-H. Tsai, J.-W. Yeh, Effect of nitrogen content and substrate bias on mechanical and corrosion properties of high-entropy films $(AlCrSiTiZr)_{100-x}N_x$, *Surf. Coat. Technol.* **206(19-20)** (2012) 4106-4112.

doi:10.6342/NTU202300667

[17] S.-Y. Chang, S.-Y. Lin, Y.-C. Huang, C.-L. Wu, Mechanical properties, deformation behaviors and interface adhesion of (AlCrTaTiZr)N_x multi-component coatings, *Surf. Coat. Technol.* **204(20)** (2010) 3307-3314.

[18] P. Cui, W. Li, P. Liu, K. Zhang, F. Ma, X. Chen, R. Feng, P.K. Liaw, Effects of nitrogen content on microstructures and mechanical properties of (AlCrTiZrHf)N high-entropy alloy nitride films, *J. Alloys Compd.* **834** (2020) 155063.

[19] L. Chen, W. Li, P. Liu, K. Zhang, F. Ma, X. Chen, H. Zhou, X. Liu, Microstructure and mechanical properties of (AlCrTiZrV)N_x high-entropy alloy nitride films by reactive magnetron sputtering, *Vacuum* **181** (2020) 109706.

[20] Z.-C. Chang, D.-C. Tsai, E.-C. Chen, Structure and characteristics of reactive magnetron sputtered (CrTaTiVZr)N coatings, *Mater. Sci. Semicond. Process.* **39** (2015) 30-39.

[21] X.H. Yan, J.S. Li, W.R. Zhang, Y. Zhang, A brief review of high-entropy films, *Mater. Chem. Phys.* **210** (2018) 12-19.

[22] M.-H. Tsai, C.-H. Lai, J.-W. Yeh, J.-Y. Gan, Effects of nitrogen flow ratio on the structure and properties of reactively sputtered (AlMoNbSiTaTiVZr)$N_x$coatings, *J. Phys. D: Appl. Phys.* **41(23)** (2008) 235402.

[23] S.-C. Liang, D.-C. Tsai, Z.-C. Chang, H.-S. Sung, Y.-C. Lin, Y.-J. Yeh, M.-J. Deng, F.-S. Shieu, Structural and mechanical properties of multi-element (TiVCrZrHf)N coatings by reactive magnetron sputtering, *Appl. Surf. Sci.* **258(1)** (2011) 399-403.

[24] Z.-C. Chang, S.-C. Liang, S. Han, Y.-K. Chen, F.-S. Shieu, Characteristics of TiVCrAlZr multi-element nitride films prepared by reactive sputtering, *Nucl. Instrum. Methods Phys. Res., Sect. B* **268(16)** (2010) 2504-2509.

[25] X. Lu, C. Zhang, C. Wang, X. Cao, R. Ma, X. Sui, J. Hao, W. Liu, Investigation of (CrAlTiNbV)N_x high-entropy nitride coatings via tailoring nitrogen flow rate for anti-wear applications in aviation lubricant, *Appl. Surf. Sci.* **557** (2021) 149813.

[26] Y. Lin, C.-L. Li, C.-H. Hsueh, Effects of cerium addition on microstructures and mechanical properties of CoCrNi medium entropy alloy films, *Surf. Coat. Technol.* **424** (2021) 127645.

[27] Y.-H. Liang, C.-L. Li, C.-H. Hsueh, Effects of Nb Addition on Microstructures and Mechanical Properties of Nb_x-CoCrFeMnNi High Entropy Alloy Films, *Coatings* **11(12)** (2021) 1539.

[28] T.-H. Huang, C.-H. Hsueh, Microstructures and mechanical properties of $(CoCrFeMnNi)_{100-x}Mo_x$ high entropy alloy films, *Intermetallics* **135** (2021) 107236.

[29] Y.-C. Hsu, C.-L. Li, C.-H. Hsueh, Modifications of microstructures and mechanical properties of CoCrFeMnNi high entropy alloy films by adding Ti element, *Surf. Coat. Technol.* **399** (2020) 126149.

doi:10.6342/NTU202300667

[30] S. Fang, C. Wang, C.-L. Li, J.-H. Luan, Z.-B. Jiao, C.-T. Liu, C.-H. Hsueh, Microstructures and mechanical properties of $CoCrFeMnNiV_x$ high entropy alloy films, *J. Alloys Compd.* **820** (2020) 153388.

[31] J. Xu, T. Wang, Y. Lu, S. Zhang, W. Wei, C. Wang, Research on high specific strength as-cast $Al_xNbTiVZr$ high entropy alloys, *Mater. Sci. Technol.* **36(16)** (2020) 1762-1770.

[32] N.D. Stepanov, N.Y. Yurchenko, D.G. Shaysultanov, G.A. Salishchev, M.A. Tikhonovsky, Effect of Al on structure and mechanical properties of $Al_xNbTiVZr$ ($x = 0$, 0.5, 1, 1.5) high entropy alloys, *Mater. Sci. Technol.* **31(10)** (2015) 1184-1193.

[33] A.I. Akira Takeuchi, Classification of Bulk Metallic Glasses by Atomic Size Difference, Heat of Mixing and Period of Constituent Elements and Its Application to Characterization of the Main Alloying Element, *Mater. Trans.* **46** (2005) 2817-2829.

[34] Y.C. Hsu, C.L. Li, C.H. Hsueh, Effects of Al Addition on Microstructures and Mechanical Properties of $CoCrFeMnNiAl_x$ High Entropy Alloy Films, *Entropy* **22(1)** (2019) 2.

[35] X.B. Feng, W. Fu, J.Y. Zhang, J.T. Zhao, J. Li, K. Wu, G. Liu, J. Sun, Effects of nanotwins on the mechanical properties of Al_x CoCrFeNi high entropy alloy thin films, *Scr. Mater.* **139** (2017) 71-76.

[36] B. Cantor, I.T.H. Chang, P. Knight, A.J.B. Vincent, Microstructural development in equiatomic multicomponent alloys, *Mater. Sci. Eng. A* **375-377** (2004) 213-218.

[37] D.B. Miracle, O.N. Senkov, A critical review of high entropy alloys and related concepts, *Acta Mater.* **122** (2017) 448-511.

[38] Z. Li, K.G. Pradeep, Y. Deng, D. Raabe, C.C. Tasan, Metastable high-entropy dual-phase alloys overcome the strength-ductility trade-off, *Nature* **534(7606)** (2016) 227-230.

[39] F. Otto, A. Dlouhý, C. Somsen, H. Bei, G. Eggeler, E.P. George, The influences of temperature and microstructure on the tensile properties of a CoCrFeMnNi high-entropy alloy, *Acta Mater.* **61(15)** (2013) 5743-5755.

[40] Y.J. Zhou, Y. Zhang, T.N. Kim, G.L. Chen, Microstructure characterizations and strengthening mechanism of multi-principal component $AlCoCrFeNiTi_{0.5}$ solid solution alloy with excellent mechanical properties, *Mater. Lett* **62(17-18)** (2008) 2673-2676.

[41] Y.J. Zhou, Y. Zhang, Y.L. Wang, G.L. Chen, Solid solution alloys of AlCoCrFeNiTix with excellent room-temperature mechanical properties, *Appl. Phys. Lett.* **90(18)** (2007) 181904.

[42] Y.Y. Zhao, Y.X. Ye, C.Z. Liu, R. Feng, K.F. Yao, T.G. Nieh, Tribological behavior

doi:10.6342/NTU202300667

of an amorphous Zr20Ti20Cu20Ni20Be20 high-entropy alloy studied using a nanoscratch technique, *Intermetallics* **113** (2019).

[43] M.-H. Chuang, M.-H. Tsai, W.-R. Wang, S.-J. Lin, J.-W. Yeh, Microstructure and wear behavior of $Al_xCo_{1.5}CrFeNi_{1.5}Ti_y$ high-entropy alloys, *Acta Mater.* **59(16)** (2011) 6308-6317.

[44] J.-M. Wu, S.-J. Lin, J.-W. Yeh, S.-K. Chen, Y.-S. Huang, H.-C. Chen, Adhesive wear behavior of $Al_xCoCrCuFeNi$ high-entropy alloys as a function of aluminum content, *Wear* **261(5-6)** (2006) 513-519.

[45] G. B, H. A, C.E.H. D, Chang, G. E.P, R. R.O, A fracture-resistant high-entropy alloy for cryogenic applications, *Sci.* **345** (2014) 1153-1158.

[46] D.H. Xiao, P.F. Zhou, W.Q. Wu, H.Y. Diao, M.C. Gao, M. Song, P.K. Liaw, Microstructure, mechanical and corrosion behaviors of AlCoCuFeNi-(Cr,Ti) high entropy alloys, *Mater. Des.* **116** (2017) 438-447.

[47] C.P. Lee, Y.Y. Chen, C.Y. Hsu, J.W. Yeh, H.C. Shih, The Effect of Boron on the Corrosion Resistance of the High Entropy Alloys $Al_{0.5}CoCrCuFeNiB_x$, *J. Electrochem. Soc.* **154(8)** (2007).

[48] Y.-J. Hsu, W.-C. Chiang, J.-K. Wu, Corrosion behavior of $FeCoNiCrCu_x$ high-entropy alloys in 3.5% sodium chloride solution, *Mater. Chem. Phys.* **92(1)** (2005) 112-117.

[49] M. Vaidya, K. Guruvidyathri, B.S. Murty, Phase formation and thermal stability of CoCrFeNi and CoCrFeMnNi equiatomic high entropy alloys, *J. Alloys Compd.* **774** (2019) 856-864.

[50] B. Schuh, F. Mendez-Martin, B. Völker, E.P. George, H. Clemens, R. Pippan, A. Hohenwarter, Mechanical properties, microstructure and thermal stability of a nanocrystalline CoCrFeMnNi high-entropy alloy after severe plastic deformation, *Acta Mater.* **96** (2015) 258-268.

[51] H. Zhang, Y.-Z. He, Y. Pan, S. Guo, Thermally stable laser cladded CoCrCuFeNi high-entropy alloy coating with low stacking fault energy, *J. Alloys Compd.* **600** (2014) 210-214.

[52] J.-W. Yeh, Alloy Design Strategies and Future Trends in High-Entropy Alloys, *Jom* **65(12)** (2013) 1759-1771.

[53] J.-W. Yeh, Physical Metallurgy of High-Entropy Alloys, *Jom* **67(10)** (2015) 2254-2261.

[54] Y. Zhang, Y.J. Zhou, J.P. Lin, G.L. Chen, P.K. Liaw, Solid-Solution Phase Formation Rules for Multi-component Alloys, *Adv. Eng. Mater.* **10(6)** (2008) 534-538.

[55] S. Guo, Q. Hu, C. Ng, C.T. Liu, More than entropy in high-entropy alloys: Forming solid solutions or amorphous phase, *Intermetallics* **41** (2013) 96-103.

doi:10.6342/NTU202300667

[56] X. Yang, Y. Zhang, Prediction of high-entropy stabilized solid-solution in multi-component alloys, *Mater. Chem. Phys.* **132(2-3)** (2012) 233-238.

[57] B.E. MacDonald, Z. Fu, B. Zheng, W. Chen, Y. Lin, F. Chen, L. Zhang, J. Ivanisenko, Y. Zhou, H. Hahn, E.J. Lavernia, Recent Progress in High Entropy Alloy Research, *Jom* **69(10)** (2017) 2024-2031.

[58] K.Y. Tsai, M.H. Tsai, J.W. Yeh, Sluggish diffusion in Co–Cr–Fe–Mn–Ni high-entropy alloys, *Acta Mater.* **61(13)** (2013) 4887-4897.

[59] P.K. Huang, J.W. Yeh, T.T. Shun, S.K. Chen, Multi-Principal-Element Alloys with Improved Oxidation and Wear Resistance for Thermal Spray Coating, *Adv. Eng. Mater.* **6(12)** (2004) 74-78.

[60] R. S, Alloyed pleasures: Multimetallic cocktails, *Curr Sci India* **10(85)** (2003) 1404-1406.

[61] Q. Wei, Q. Shen, J. Zhang, B. Chen, G. Luo, L. Zhang, Microstructure and mechanical property of a novel ReMoTaW high-entropy alloy with high density, *Int. J. Refract. Met. Hard Mater.* **77** (2018) 8-11.

[62] X.W. Nie, M.D. Cai, S. Cai, Microstructure and mechanical properties of a novel refractory high entropy alloy HfMoScTaZr, *Int. J. Refract. Met. Hard Mater.* **98** (2021) 105568.

[63] W. Li, P. Liu, P.K. Liaw, Microstructures and properties of high-entropy alloy films and coatings: a review, *Mater. Res. Lett.* **6(4)** (2018) 199-229.

[64] S.K. Padamata, A. Yasinskiy, V. Yanov, G. Saevarsdottir, Magnetron Sputtering High-Entropy Alloy Coatings: A Mini-Review, *Metals* **12(2)** (2022) 319.

[65] H. Ju, P. Jia, J. Xu, L. Yu, Y. Geng, Y. chen, M. Liu, T. Wei, The effects of adding aluminum on crystal structure, mechanical, oxidation resistance, friction and wear properties of nanocomposite vanadium nitride hard films by reactive magnetron sputtering, *Mater. Chem. Phys.* **215** (2018) 368-375.

[66] H. Ju, N. Ding, J. Xu, L. Yu, I. Asempah, J. Xu, G. Yi, B. Ma, Crystal structure and the improvement of the mechanical and tribological properties of tungsten nitride films by addition of titanium, *Surf. Coat. Technol.* **345** (2018) 132-139.

[67] N. Arshi, J. Lu, Y.K. Joo, C.G. Lee, J.H. Yoon, F. Ahmed, Study on structural, morphological and electrical properties of sputtered titanium nitride films under different argon gas flow, *Mater. Chem. Phys.* **134(2-3)** (2012) 839-844.

[68] P.-K. Huang, J.-W. Yeh, Effects of substrate temperature and post-annealing on microstructure and properties of (AlCrNbSiTiV)N coatings, *Thin Solid Films* **518(1)** (2009) 180-184.

[69] T.-G. Wang, Y. Liu, T. Zhang, D.-I. Kim, K.H. Kim, Influence of Nitrogen Flow Ratio on the Microstructure, Composition, and Mechanical Properties of DC Magnetron Sputtered Zr–B–O–N Films, *J. Mater. Sci. Technol.* **28(11)** (2012) 981-

doi:10.6342/NTU202300667

991.

[70] S. Zhang, X. Zhang, Toughness evaluation of hard coatings and thin films, *Thin Solid Films* **520(7)** (2012) 2375-2389.

[71] J. Chen, S.J. Bull, Assessment of the toughness of thin coatings using nanoindentation under displacement control, *Thin Solid Films* **494(1-2)** (2006) 1-7.

[72] C.-W. Tsai, S.-W. Lai, K.-H. Cheng, M.-H. Tsai, A. Davison, C.-H. Tsau, J.-W. Yeh, Strong amorphization of high-entropy AlBCrSiTi nitride film, *Thin Solid Films* **520(7)** (2012) 2613-2618.

[73] A. Inoue, High strength Bulk Amorphous Alloys with Low Critical Cooling Rates, *Mater. Trans.* **36(7)** (1995) 866-875.

[74] M. Ghidelli, S. Gravier, J.-J. Blandin, J.-P. Raskin, F. Lani, T. Pardoen, Size-dependent failure mechanisms in ZrNi thin metallic glass films, *Scr. Mater.* **89** (2014) 9-12.

[75] C. Lin Li, Notch toughness evaluations of thin film metallic glasses using FIB-based microcantilever method: A comparison study with crystalline thin films, (2017).

[76] F.T. Muniz, M.A. Miranda, C. Morilla Dos Santos, J.M. Sasaki, The Scherrer equation and the dynamical theory of X-ray diffraction, *Acta Crystallogr., Sect. A: Found. Adv.* **72(Pt 3)** (2016) 385-390.

[77] N. Saowadee, K. Agersted, J.R. Bowen, Lattice constant measurement from electron backscatter diffraction patterns, *J. Microsc.* **266(2)** (2017) 200-210.

[78] D.-C. Tsai, Z.-C. Chang, B.-H. Kuo, S.-Y. Chang, F.-S. Shieu, Effects of silicon content on the structure and properties of (AlCrMoTaTi)N coatings by reactive magnetron sputtering, *J. Alloys Compd.* **616** (2014) 646-651.

[79] V.V. Kosukhin, V.F. Funke, V.I. Minashkin, V.S. Smirnov, Y.P. Efremov, Zirconium nitride and carbonitride coatings obtained by the chemical vapor deposition (CVD) method, *Inorg. Mater.* **23:1** (1987) 52-56.

[80] W. Lengauer., P. Ettmayer., Preparation and Properties of Compact Cubic *δ*-NbN(l-*x*), *Monatsh. Chem.* **117** (1986) 275-286.

[81] Muneshwar, Triratna, Cadien, Ken, Comparing XPS on bare and capped ZrN films grown by plasma enhanced ALD: Effect of ambient oxidation, *Appl. Surf. Sci.* **435** (2018) 367-376.

[82] S. Oktay, Z. Kahraman, M. Urgen, K. Kazmanli, XPS investigations of tribolayers formed on TiN and (Ti,Re)N coatings, *Appl. Surf. Sci.* **328** (2015) 255-261.

[83] P. Motamedi, K. Cadien, XPS analysis of AlN thin films deposited by plasma enhanced atomic layer deposition, *Appl. Surf. Sci.* **315** (2014) 104-109.

[84] F. Cheng, C. He, D. Shu, H. Chen, J. Zhang, S. Tang, D.E. Finlow, Preparation of

doi:10.6342/NTU202300667

nanocrystalline VN by the melamine reduction of V2O5 xerogel and its supercapacitive behavior, *Mater. Chem. Phys.* **131(1-2)** (2011) 268-273.

[85] I. Bertoti, Characterization of nitride coatings by XPS, *Surf. Coat. Technol.* (2002) 151–152, 194–203.

[86] A. Darlinski., J. Halbritter., Angle-resolved XPS Studies of Oxides at NbN, NbC, andl Nb Surfaces, *Surf. Interface Anal.* **10** (1987) 223-237

[87] N. Huber, T. Beirau, Modelling the effect of intrinsic radiation damage on mechanical properties: The crystalline-to-amorphous transition in zircon, *Scr. Mater.* **197** (2021) 113789.

[88] M. Zhao, J.C. Li, Q. Jiang, Hall–Petch relationship in nanometer size range, *J. Alloys Compd.* **361(1-2)** (2003) 160-164.

[89] N. Wang, Q.P. Cao, X.D. Wang, D.X. Zhang, J.Z. Jiang, Tuning microstructure and enhancing mechanical properties of Co-Ni-V-Al medium entropy alloy thin films via deposition power, *J. Alloys Compd.* **875** (2021) 160003.

[90] S.N. Naik, S.M. Walley, The Hall–Petch and inverse Hall–Petch relations and the hardness of nanocrystalline metals, *J. Mater. Sci.* **55(7)** (2019) 2661-2681.

[91] G. Wu, K.C. Chan, L. Zhu, L. Sun, J. Lu, Dual-phase nanostructuring as a route to high-strength magnesium alloys, *Nature* **545(7652)** (2017) 80-83.

[92] G. Abadias, S. Dub, R. Shmegera, Nanoindentation hardness and structure of ion beam sputtered TiN, W and TiN/W multilayer hard coatings, *Surf. Coat. Technol.* **200(22-23)** (2006) 6538-6543.

[93] Z. Han, X. Hu, J. Tian, G. Li, G. Mingyuan, Magnetron sputtered NbN thin films and mechanical properties, *Surf. Coat. Technol.* **179(2-3)** (2004) 188-192.

[94] A.P. Knights., A.S. Saleh., P.C. Rice-Evans., F.E. S J Bull, R.a.H. Kupfer., Investigation of magnetron-sputtered titanium nitride films using positron annihilation spectroscopy, *J. Phys.: Condens. Matter* **8** (1996) 2479–2486.

[95] F. Liu, Y. Meng, R. Zhaoxing, X. Shu, Microstructure, Hardness and Corrosion Resistance of ZrN Films Prepared by Inductively Coupled Plasma Enhanced RF Magnetron Sputtering, *Plasma Sci. Technol.* **10** (2008) 2.

[96] W. Zhang, W. Li, H. Zhai, Y. Wu, S. Wang, G. Liang, R.J.K. Wood, Microstructure and tribological properties of laser in-situ synthesized Ti_3Al composite coating on Ti-6Al-4V, *Surf. Coat. Technol.* **395** (2020) 125944.

[97] X.C. Zhang, Z.D. Liu, J.S. Xu, F.Z. Xuan, Z.D. Wang, S.T. Tu, Synthesis of TiN/Ti_3Al composite coatings on Ti6Al4V alloy by plasma spraying and laser nitriding, *Surf. Coat. Technol.* **228** (2013) 107-110.

[98] S. Zhang, D. Sun, Y. Fu, H. Du, Toughening of hard nanostructural thin films: a critical review, *Surf. Coat. Technol.* **198(1-3)** (2005) 2-8.

[99] H. Zhao, L. Yu, C. Mu, F. Ye, Structure and properties of Si-implanted VN

doi:10.6342/NTU202300667

coatings prepared by RF magnetron sputtering, *Mater. Charact.* **117** (2016) 65-75.

[100] H. Ju, L. Yu, S. He, I. Asempah, J. Xu, Y. Hou, The enhancement of fracture toughness and tribological properties of the titanium nitride films by doping yttrium, *Surf. Coat. Technol.* **321** (2017) 57-63.

[101] T.-P. Hsiao, Y.-C. Yang, J.-W. Lee, C.-L. Li, J.P. Chu, The microstructure and mechanical properties of nitrogen and boron contained ZrCuAlNi thin film metallic glass composites, *Surf. Coat. Technol.* **237** (2013) 276-283.

[102] S. Kataria, S.K. Srivastava, P. Kumar, G. Srinivas, Siju, J. Khan, D.V.S. Rao, H.C. Barshilia, Nanocrystalline TiN coatings with improved toughness deposited by pulsing the nitrogen flow rate, *Surf. Coat. Technol.* **206(19-20)** (2012) 4279-4286.

[103] J.-W. Lee, J.-G. Duh, Nanomechanical properties evaluation of chromium nitride films by nanoindentation and nanowear techniques, *Surf. Coat. Technol.* **188-189** (2004) 655-661.

doi:10.6342/NTU202300667